Self-assembly synthesis of a [2]catenane Co(II) single-molecule magnet

Benjamin H. Wilson, Jas S. Ward, David C. Young, Jun-Liang Liu, Corine Mathonière, Rodolphe Clérac* and Paul E. Kruger**

We describe herein the self-assembly synthesis of an octanuclear Co^{II} [2]catenane $\{[Co_4(\mathbf{H_2L})_6]_2^{16+}\}$ formed by the mechanical interlocking of two $\{[Co_4(\mathbf{H_2L})_6]^{8+}\}$ rectangles of unprecedented topology. Subtle manipulation of the synthetic conditions allows the isolation of a mixed-valence $[Co_2^{III}/Co_2^{II}]^{10+}$ non-catenated rectangle. The Co^{II} centers in the [2]catenane exhibit slow relaxation of their magnetic moment, i.e. single-molecule magnet properties, dominated by quantum tunneling and Raman relaxation processes. This work shows that metallo-supramolecular chemistry can precisely control the organization of single-molecule magnets in topologically complex arrangements.

The synthesis of mechanically interlocked molecules has long been the pique of supramolecular chemists. Since Sauvage and co-workers pioneered the template-assisted synthesis of aesthetically appealing interlocked molecules,[1] many variations of catenanes, rotaxanes, and knots have been reported.[2] A driving force behind this research centers upon the application of these interlocked assemblies as nano-scale molecular machines.[3,4] Innovative work by Fujita and co-workers established the use of metal–ligand self-assembly to produce so-called "magic ring" catenanes: two metallocycles which spontaneously catenate under specific conditions. This approach allows for the one-pot synthesis of metallo-catenanes[5] and more recently catenanes based on interlocking 2×2 grids[6] among other types of metallo-supramolecular structures.[7] Further, Leigh and co-workers have adapted the approach to form metallo-supramolecular grids which act as templates[8] for the synthesis of topologically complex molecular knots.[9]

[*] Dr. B. H. Wilson, Dr. J. S. Ward, Dr. D. C. Young, Prof. P. E. Kruger
MacDiarmid Institute for Advanced Materials and Nanotechnology,
School of Physical and Chemical Sciences
University of Canterbury
Private Bag 4800, Christchurch 8041 (New Zealand)
E-mail: Ben.Wilson@ul.ie
paul.kruger@canterbury.ac.nz

Dr. J.-L. Liu, Prof. C. Mathonière, Dr. R. Clérac
Univ. Bordeaux, CNRS, Centre de Recherche Paul Pascal, UMR 5031, 33600 Pessac (France)
E-mail: clerac@crpp-bordeaux.cnrs.fr

Dr. B. H. Wilson
Current address
Bernal Institute, University of Limerick
Limerick, V94 T9PX (Ireland)

The incorporation of transition-metal ions into mechanically interlocked assemblies enables the introduction of additional properties into the super-structure such as redox, luminescence and magnetism. The latter is of particular interest as some transition-metal ions in metallo-supramolecular assemblies can display slow paramagnetic relaxation to yield single-molecule magnets (SMMs).[10,11] Research in the field of SMMs is prolific and stimulated by the potential application of these molecules in nanoscale data storage and spintronic devices.[12–14] A sub-class of these materials is known as mononuclear SMMs, for which the slow relaxation of magnetization is intrinsic to a single metal ion in a complex and not due to magnetically coupled spin systems. Co^{II} has emerged as one of the key 3d metal ions for generating SMM assemblies as it possesses high magnetic anisotropy, which favors thermally activated relaxation of the magnetization.[15] Interestingly, Winpenny and co-workers exploited the ring architecture of a polymetallic inorganic macrocycle to synthesize mechanically interlocked molecules to form rotaxane structures, which behaved as molecular electron spin qubits.[16] More recently they extended these to more complex mechanically interlocked arrays such as daisy-chains,[17] interlocked double chains[18] and [2]rotaxanes as ligands.[19] By using mechanically interlocked systems with intricate topologies, many SMM active centers can be specifically arranged in complex arrays. Herein, we report the use of a rigid ditopic ligand bearing 3-(2-pyridyl)-1,2,4-triazole coordinating motifs which, upon complexation with Co^{II} ions, generates a catenated metallo-supramolecular assembly. This catenated structure exhibits slow magnetization dynamics intrinsic to the individual Co^{II} sites and is the first catenane to exhibit SMM behavior.

The 1,2-bis(5-(2-pyridyl)-4*H*-1,2,4-triazol-3-yl)-benzene ligand, $\mathbf{H_2L}$, (Figure 1) was synthesized following literature procedures[20] (see the Supporting Information) and is relatively insoluble in all common laboratory solvents. However, a solution could be obtained in the presence of a metal salt. The addition of two equivalents of cobalt(II) perchlorate to a stirred suspension of three equivalents of

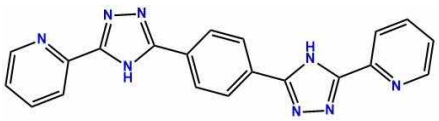

Figure 1. The rigid ditopic ligand 1,2-bis(5-(2-pyridyl)-4*H*-1,2,4-triazol-3-yl)-benzene, $\mathbf{H_2L}$.

$\mathbf{H_2L}$ in nitromethane resulted in an orange solution after gentle heating (50 °C) for several hours. Addition of an aqueous solution of lithium bromide, followed by vapor diffusion of chloroform to the nitromethane solution over a period of two days, yielded orange lozenge-shaped crystals of $\{[Co_4(\mathbf{H_2L})_6]_2^{16+}\}$, **1**, suitable for a single-crystal X-ray diffraction study (Figure 2).

The diffraction data collected at 120 K was solved and refined in the tetragonal space group $I4_1/a$ (Table S1). The asymmetric unit is comprised of two octahedral Co^{II} centers and three $\mathbf{H_2L}$ ligands (Figure S3). Two ligands coordinate to the Co^{II} centers in a bidentate fashion via the pyridine nitrogen atom and the N-2 nitrogen atom of the triazole ring. The third ligand coordinates via the pyridine nitrogen atom and the N-4 nitrogen atom of the triazole ring (Figure S2). The Co–N bond lengths and corresponding N–Co–N bond angles are indicative of high-spin Co^{II} centers, which are noticeably distorted from idealized octahedral symmetry as evidenced by the octahedral distortion parameters (Table S2).[21] The action of a 2-fold rotation generates a $\{[Co_4(\mathbf{H_2L})_6]^{8+}\}$ molecular rectangle of unique topology.[22] Two sides of the rectangle are made up of two ligands with twisted conformation which π–π stack to form a "double pillar" and bridge two Co^{II} centers (Figures 2 and S4). The remaining two sides of the rectangle are made up of a single ligand strand bridging two Co^{II} centers. These ligands adopt a *trans*-conformation where the two bidentate binding sites are oriented in opposite directions (Figures 2, S2 and S3). The Co…Co separations on the double pillared sides of the rectangle are shorter (ca. 10.9 Å) than those on the sides with the single ligand strand (ca. 14.0 Å). A symmetrically equivalent rectangle is generated by the action of a 4-fold roto-inversion parallel to the crystallographic *c* axis. The two symmetry-equivalent rectangles mechanically interlink to form a [2]catenane, $\{[Co_4(\mathbf{H_2L})_6]_2^{16+}\}$, such that the double pillared sides of one rectangle occupy the cavity of the other (Figures 1, S5 and S6). The interlinking of two $\{[Co_4(\mathbf{H_2L})_6]^{8+}\}$ rectangles is supported by a plethora of π–π stacking and edge-to-face (C)H···π interactions (Figures S4, S5 and S6). The overall +16 charge of the [2]catenane is compensated by nine bromide and seven perchlorate anions, many of which exhibit significant disorder and are modelled as partial occupancy. A cavity is formed inside the [2]catenane and is occupied by a bromide anion which is disordered equally over four positions. The triazole N–H moieties of $\mathbf{H_2L}$ orient into the cavity of the catenane and interact with the bromide anions via (N)H···Br hydrogen bonds (Figure S6). Crystals of **1** did not form in the absence of bromide potentially indicating its templating role in the formation of the [2]catenane. Further hydrogen-bonding interactions are evident about the periphery of **1** and throughout the crystal lattice (Figures S7, S8 and Table S3).

The electrospray mass spectrum of crystals of **1** redissolved in acetonitrile showed a peak corresponding to a non-catenated structure $\{(Co_4(\mathbf{H_2L})_6)\text{-}5H\}^{3+}$, **2**. The occurrence of smaller peaks evenly spaced between the main peaks corresponding to this non-catenated structure indicates the occurrence of a minor species with a +6 charge. This can be attributed to the catenated structure $\{(Co_4(\mathbf{H_2L})_6)_2\text{-}10H\}^{6+}$, (Figure S1). This result indicates that in solution, under the conditions of the mass-spectrometry experiment, a non-catenated structure is present. Indeed, the coordination of the triazole rings results in the N–H hydrogen atoms being sufficiently acidic that they are lost during the ionization process to minimize the charge density of the complex. Much effort was made to isolate this non-catenated species and success was finally achieved when the nitromethane solution of **1** was spiked with 50 μL of m-xylene and subsequent vapor diffusion of chloroform. After several days, orange lozenge-shaped crystals of **1** formed, and after several weeks, orange plate crystals grew on top of the previously formed crystals. Single-crystal X-ray diffraction revealed that the orange plate crystals were a non-catenated complex, $\{[Co_4(\mathbf{H_2L})_6]^{n+}\}$, **2** (Figure S9). Crystals of **2** only ever formed as a minor product in the presence of **1**, so bulk phase analysis on **2** was not possible.

Complex **2** crystallized in the monoclinic space group $P2_1/c$ (Table S1). The asymmetric unit contains a complete tetranuclear cobalt complex, which now forms a square motif, along with a multitude of disordered bromide, perchlorate anions and solvents of crystallization (Figure S9). As with the structure of **1**, two pyridyl-1,2,4-triazole motifs coordinate via the N-2 nitrogen atom of the triazole,

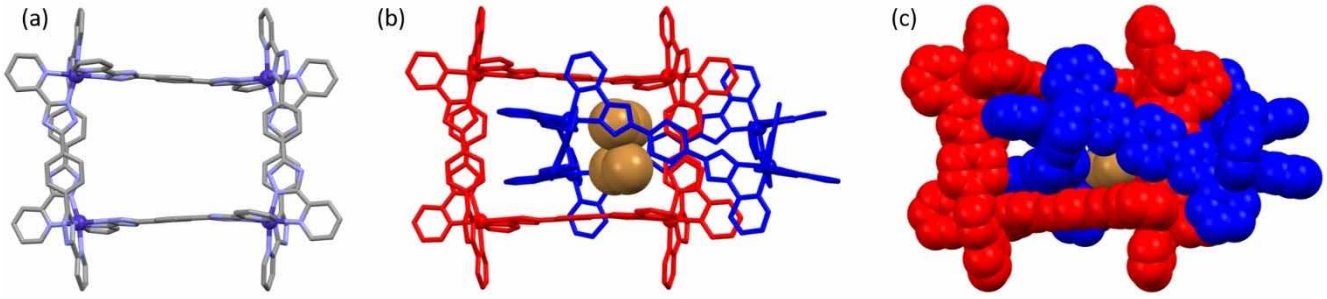

Figure 2. a) Single-crystal X-ray structure of **1** showing a single $\{[Co_4(\mathbf{H_2L})_6]^{8+}\}$ rectangle. The double pillared sides are bridged by two $\mathbf{H_2L}$ ligands (left/right) while the single pillared sides are bridged by a single $\mathbf{H_2L}$ ligand (top/bottom). b) Structure of the [2]catenane $\{[Co_4(\mathbf{H_2L})_6]_2^{16+}\}$ showing an encapsulated bromide anion disordered over four-positions. c) Space-filling representation of the [2]catenane $\{[Co_4(\mathbf{H_2L})_6]_2^{16+}\}$ showing the two interlinked $\{[Co_4(\mathbf{H_2L})_6]^{8+}\}$ rectangles (blue and red) with an encapsulated bromide anion disordered over four-positions. Selected anions and solvent molecules omitted for clarity; cobalt = purple, carbon = grey, nitrogen = pale blue, bromide = orange.

while the third coordinates via the N-4 nitrogen atom. From consideration of the bond lengths and angles about each cobalt center, it is best concluded that Co(1) and Co(3) are Co^{III}, whereas Co(2) and Co(4) are Co^{II} (Table S4), with oxidation most likely occurring during the prolonged crystallization time. Unlike **1**, the single ligand stranded sides of **2** feature the ligands now coordinating in *syn*-fashion, with the bidentate binding sites orientated in the same direction (Figures S2 and S9). The ligands of the double pillared sides in **2** are arranged similarly to those of **1** and are stabilized by π–π stacking interactions. Ligand coordination in **2** results in a more compacted structure with the four Co centers arranged in a distorted square topology (Figure S10). The Co…Co separations on the double pillared sides of the square are comparable to those in **1** (ca. 10.7 Å), whereas those on the sides with the single ligand stranded sides are considerably shorter (ca. 10.3 Å). This ca. 4 Å shortening reduces the size of the cavity and its aperture, and does not permit the formation of a [2] catenane. The cavity contains disordered partial occupancy bromide and perchlorate anions. Two bromide anions hydrogen bond to triazole N–H moieties, on the ligands that make up the inner strands of the rectangle, in a bridging manner (Figure S12). Three of the peripheral triazole protons hydrogen bond to bromide and perchlorate anions with (N)H···A (Figure S12, Table S5). The squares pack closely together, stabilized by π–π stacking interactions between the pyridine ring of one ligand and the central phenyl spacer of another (Figure S13).

Isolated Co^{II} centers have shown promise as candidates for SMM properties. Therefore, an in-depth analysis of the magnetic behavior was carried out. Magnetic measurements were performed on polycrystalline samples of **1**, first frozen in its mother liquor and then subsequently dried (see Supporting Information for specific experimental details; Figures 3 and S14). As both sets of measurements were virtually identical, the magnetic data shown herein are those collected on the dried sample. The χT product at 250 K is slightly higher (15.5 $cm^3 K mol^{-1}$) than what is expected for eight magnetically isolated $S = 3/2$ spin centers (15 $cm^3 K mol^{-1}$), indicating a small orbital contribution to the magnetic moment of the Co^{II} centers. The gradual decrease of the χT product from 200 K suggests the depopulation of low-lying excited states. This could be attributed to either the magnetic anisotropy of the spin carriers or antiferromagnetic interactions between the Co^{II} centers. When considering the large separations between the Co^{II} centers in the catenane, the magnetic coupling is expected to be negligible. The decrease in the χT product can therefore be attributed to the intrinsic magnetic anisotropy of the Co^{II} sites. The isothermal dc field (H) dependence of the magnetization (M) up to 7 T was measured below 8 K (inset Figure 3 and Figure S14). Saturation is not reached at 1.85 K, even with an applied field of 7 T, with a measured magnetization of 12.7 μ_B. This is approximately half of the theoretical saturation of magnetization of 24 μ_B for eight isolated $S = 3/2$ spin-only centers ($g = 2.0$).

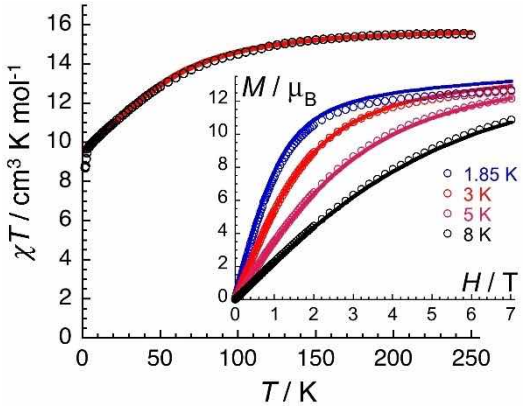

Figure 3. Temperature dependence of the χT product (where χ is the molar magnetic susceptibility that equals M/H per complex, and T the temperature) collected in an applied dc magnetic field of 0.1 T for **1**. Inset: Field dependence of the magnetization for **1** below 8 K. The solid lines are the best fits to the model described in the text.

This result in conjunction with the non-superposition of the M vs. HT^{-1} curves (Figure S14) confirms the presence of a large magnetic anisotropy as expected for Co^{II}-based complexes. The χT vs. T and M vs. H data can be simultaneously fitted with the phenomenological Hamiltonian as follows $\widehat{H} = D\widehat{S}_z^{\,2} + g\mu_B\widehat{S}H$, resulting in an isotropic g value of 2.06(1) and an axial zero-field splitting parameter, $D/hc = -60.2(4)$ cm^{-1} (−86.6(6) K; Figure 3). The magnetization dynamics and the possible presence of SMM behavior in **1** was probed by ac magnetic susceptibility measurements. At 1.9 K and in the absence of a dc field, the in-phase ac susceptibility (χ') is frequency independent up to 10 kHz in agreement with the absence of an out-of-phase component (χ''). Upon application of a dc field, an out-of-phase signal is detected, and both components exhibit frequency and temperature dependent behavior. This verifies that **1** displays a slow relaxation of its magnetic moment and can therefore be regarded as a SMM (Figures S15–S18). The field dependence at 1.9 K (Figure S15) and the temperature dependence at 1000 Oe (Figure S17) of the ac susceptibility were thoroughly studied. The corresponding χ' vs. ν and χ'' vs. ν data were fit to a generalized Debye model[23] in order to extract the field dependence (at 1.9 K) and the temperature dependence (at 1000 Oe) of the relaxation time, τ (Figure 4; as well as all the other parameters of the generalized Debye model:[23] α, ν, χ_0', χ_∞' and $\chi_0'-\chi_\infty'$; Figures S16 and S18). The estimated standard deviations (ESD) of the relaxation time (vertical solid bars in Figure 4) calculated from the α parameter (which quantify the broadness of the relaxation time distribution)[23,24] are immediately informative on the necessary caution that should be taken when analyzing these variations.

Four main mechanisms, which include quantum tunneling of the magnetization (QTM),[11a,c] thermally activated (i.e. Arrhenius),[11c,12a,25] Raman[25,26] and direct[26] relaxation processes, are usually involved in the paramagnetic relaxation. The relaxation rate (τ^{-1}) can be then summarized by Equations (1) and (2), which contain four corresponding

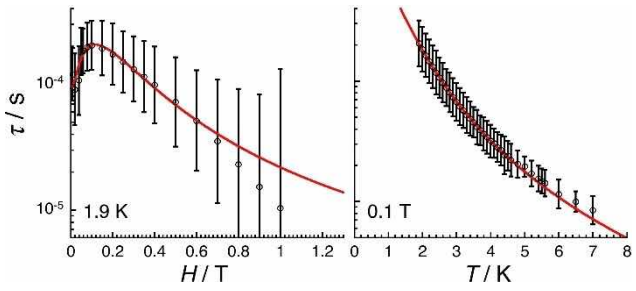

Figure 4. Field (left) and temperature (right) dependence of the relaxation time for **1** estimated from the generalized Debye fits of the ac susceptibility data shown in Figures S15 and S17. The ESD of the relaxation time (vertical solid bars) have been calculated from the α parameters of the generalized Debye fit (Figures S15–S18) and the log-normal distribution as described in reference [24]. The solid red lines are the best fit discussed in the text.

terms, which have their own temperature and dc-field dependence:

$$\tau^{-1} = \tau^{-1}_{\text{Raman}} + \tau^{-1}_{\text{Direct}} + \tau^{-1}_{\text{Arrhenius}} + \tau^{-1}_{\text{QTM}} \quad (1)$$

$$\tau^{-1} = C\frac{1 + C_1H^2}{1 + C_2H^2}T^n + ATH^4 + \tau_0^{-1}\exp\left(-\frac{\Delta}{k_BT}\right) + \frac{B_1}{1 + B_2H^2} \quad (2)$$

The field dependence of the relaxation time (left part of Figure 4) exhibits an increase between 0 and 1000 Oe, compatible with either QTM or Raman (with $C_2 > C_1$) mechanisms. At higher fields, a decrease is observed with an H^{-3} variation above 5000 Oe, which is not perfectly compatible with either a direct relaxation (H^{-4}) or a Raman mechanism (H^{-2} with $C_2 \ll C_1$). Thus, the τ vs. H and τ vs. T data shown in Figures 4 and S20 have been fitted by two simple models including i) Raman and direct and ii) QTM and Raman processes. Considering the ESD of the relaxation time, additional processes were not necessary to provide a satisfactory agreement between the theory and experimental data. It is worth mentioning that above 4 K, the $\ln(\tau)$ vs. T^{-1} plot (Figure S19) experiences a linear variation, which could be compatible with a thermally activated Orbach relaxation process (with a pre-exponential factor, τ_0, of $1.6(5)\times10^{-6}$ s and an energy gap of 12(2) K). However, the energy gap between $\pm1/2$ and $\pm3/2$ states estimated by fitting of dc magnetic data should be $2D/k_B \approx 173$ K, which is an order of magnitude higher than the above estimated energy gap. This suggests that the observed relaxation cannot be influenced by an Orbach process in the explored temperature window. The relaxation time of **1** is reproduced well by the two relaxation models with a slightly better agreement at low fields when Raman and direct relaxation processes are considered (Figures 4 and S20; with $B_1 = 7199(500)\ \text{s}^{-1}$, $B_2 = 695(200)\ \text{T}^{-2}$, $C = 628(88)\ \text{K}^{-2.7}\text{s}^{-1}$, $C_1 = 13(5)\ \text{T}^{-2}$ and $C_2 = 0.05(5)\ \text{T}^{-2}$ and $n = 2.7(5)$). It is necessary to underline that the presence of other relaxation processes cannot be excluded in **1** but the experimental ac data do not allow for their detection. Therefore, the present analysis of the relaxation time should be taken with caution even if it suggests that the observed SMM properties in **1** are originating mainly from Raman and direct processes.

The aforementioned results demonstrate an exciting new method in which SMM behavior can be incorporated into mechanically interlocked molecules. The [2]catenane structure reported is the first such example based on an $\{[Co_4(\mathbf{H_2L})_6]^{8+}\}$ rectangle complex of an unprecedented topology and exemplifies the importance of understanding weak supramolecular interactions for the synthesis of self-assembled mechanically interlocked molecules. Furthermore, the structure can also exist as the non-interlocked square as shown by the isolation of the non-catenated square structure, **2**. Combined dc and ac magnetic susceptibility measurements revealed that **1** displayed slow relaxation of magnetization and therefore behaves as a SMM. Such behavior demonstrates a proof of concept for the arrangement of multiple SMM centers into a complex topology by exploiting metallo-supramolecular mechanically interlocked systems. This may provide an important step in the synthesis of magnetically active molecular machines.

The authors gratefully acknowledge the Royal Society of New Zealand Marsden Fund; the Dumont d'Urville NZ-France Science & Technology Support Programme; the New Zealand France Friendship Fund for the award of an Excellence Scholarship to B.H.W. and the MacDiarmid Institute for financial support. The University of Bordeaux, the CNRS, the Région Nouvelle Aquitaine and the Quantum Matter Bordeaux program are also thanked for their financial support. B.H.W. gratefully acknowledges the receipt of the Roper Scholarship (UC).

[1] a) M. Cesario, C. O. Dietrich-Buchecker, J. Guilhem, C. Pascard, J.-P. Sauvage, *Chem. Commun.* **1985**, 244–247; b) C. Dietrich-Buchecker, J.-P. Sauvage, *Tetrahedron* **1990**, *46*, 503–512; c) C. O. Dietrich-Buchecker, J.-P. Sauvage, *Chem. Rev.* **1987**, *87*, 795–810; d) C. O. Dietrich-Buchecker, J.-P. Sauvage, J.-M. Kern, *J. Am. Chem. Soc.* **1984**, *106*, 3043–3045; e) C. O. Dietrich-Buchecker, J.-P. Sauvage, J.-P. Kintzinger, *Tetrahedron Lett.* **1983**, *24*, 5095–5098; f) J.-P. Sauvage, *Acc. Chem. Res.* **1990**, *23*, 319–327.

[2] a) D. B. Amabilino, J. F. Stoddart, *Chem. Rev.* **1995**, *95*, 2725–2828; b) J.-F. Ayme, J. E. Beves, C. J. Campbell, D. A. Leigh, *Chem. Soc. Rev.* **2013**, *42*, 1700–1712; c) J. D. Crowley, S. M. Goldup, A.-L. Lee, D. A. Leigh, R. T. McBurney, *Chem. Soc.*

Rev. **2009**, *38*, 1530–1541; d) C. O. Dietrich-Buchecker, J.-F. Nierengarten, J.-P. Sauvage, *Tetrahedron Lett.* **1992**, *33*, 3625–3628; e) L. Fang, M. A. Olson, D. Benitez, E. Tkatchouk, W. A. Goddard III, J. F. Stoddart, *Chem. Soc. Rev.* **2010**, *39*, 17–29; f) R. S. Forgan, J.-P. Sauvage, J. F. Stoddart, *Chem. Rev.* **2011**, *111*, 5434–5464; g) F. M. Raymo, J. F. Stoddart, *Chem. Rev.* **1999**, *99*, 1643–1664; h) J.-F. Ayme, J. E. Beves, D. A. Leigh, R. T. McBurney, K. Rissanen, D. Schultz, *Nat. Chem.* **2012**, *4*, 15–20.

[3] a) V. Balzani, A. Credi, F. M. Raymo, J. F. Stoddart, *Angew. Chem. Int. Ed.* **2000**, *39*, 3348–3391; *Angew. Chem.* **2000**, *112*, 3484–3530; b) V. Balzani, M. Gómez-López, J. F. Stoddart, *Acc. Chem. Res.* **1998**, *31*, 405–414; c) B. Champin, P. Mobian, J.-P. Sauvage, *Chem. Soc. Rev.* **2007**, *36*, 358–366; d) J.-P. Collin, C. Dietrich-Buchecker, P. Gaviña, M. C. Jimenez-Molero, J.-P. Sauvage, *Acc. Chem. Res.* **2001**, *34*, 477–487; e) M. C. Jiménez, C. Dietrich-Buchecker, J.-P. Sauvage, *Acc. Chem. Res.* **2000**, *39*, 3284–3287; f) S. Saha, J. F. Stoddart, *Chem. Soc. Rev.* **2007**, *36*, 77–92; g) J.-P. Sauvage, *Acc. Chem. Res.* **1998**, *31*, 611–619; h) B. Lewandowski, G. De Bo, J. W. Ward, M. Papmeyer, S. Kuschel, M. J. Aldegunde, P. M. E. Gramlich, D. Heckmann, S. M. Goldup, D. M. D'Souza, A. E. Fernandes, D. A. Leigh, *Science* **2013**, *339*, 189–193; i) B. H. Wilson, S. J. Loeb, *Chem* **2020**, *6*, 1604–1612.

[4] D. A. Leigh, *Angew. Chem. Int. Ed.* **2016**, *55*, 14506–14508; *Angew. Chem.* **2016**, *128*, 14722–14724.

[5] a) M. Fujita, *Acc. Chem. Res.* **1999**, *32*, 53–61; b) M. Fujita, F. Ibukuro, H. Hagihara, K. Ogura, *Nature* **1994**, *367*, 720–723; c) M. Fujita, K. Ogura, *Supramol. Sci.* **1996**, *3*, 37–44; d) M. Fujita, K. Ogura, *Coord. Chem. Rev.* **1996**, *148*, 249–264.

[6] a) T. S. M. Abedin, L. K. Thompson, D. O. Miller, *Chem. Commun.* **2005**, 5512–5514; b) C. Giri, F. Topic, M. Cametti, K. Rissanen, *Chem. Sci.* **2015**, *6*, 5712–5718; c) T. J. Burchell, D. J. Eisler, R. J. A. Puddephatt, *Dalton Trans.* **2005**, 268–272; d) N. Liu, S.-L. Huang, X. Liu, H.-K. Luo, T. S. Hor, *Chem. Commun.* **2017**, *53*, 12802–12805; e) A. Westcott, J. Fisher, L. P. Harding, P. Rizkallah, M. J. Hardie, *J. Am. Chem. Soc.* **2008**, *130*, 2950–2951.

[7] a) M. Frank, J. Hey, I. Balcioglu, Y.-S. Chen, D. Stalke, T. Suenobu, S. Fukuzumi, H. Frauendorf, G. H. Clever, *Angew. Chem. Int. Ed.* **2013**, *52*, 10102–10106; *Angew. Chem.* **2013**, *125*, 10288–10293; b) M. Frank, M. D. Johnstone, G. H. Clever, *Chem. Eur. J.* **2016**, *22*, 14104–14125; c) M. Fujita, N. Fujita, K. Ogura, K. Yamaguchi, *Nature* **1999**, *400*, 52–55; d) M. Han, D. M. Engelhard, G. H. Clever, *Chem. Soc. Rev.* **2014**, *43*, 1848–1860; e) D. Preston, A. R. Inglis, A. L. Garden, P. E. Kruger, *Chem. Commun.* **2019**, *55*, 13271–13274; f) T. K. Ronson, Y. Wang, K. Baldridge, J. S. Siegel, J. R. Nitschke, *J. Am. Chem. Soc.* **2020**, *142*, 10267–10272.

[8] a) D. A. Leigh, J. J. Danon, S. D. P. Fielden, J.-F. Lemonnier, G. F. S. Whitehead, S. L. Woltering, *Nat. Chem.* **2021**, *13*, 117–122; b) D. Preston, P. E. Kruger, *Nat. Chem.* **2021**, *13*, 114–116; c) D. P. August, R. A. W. Dryfe, S. J. Haigh, P. R. C. Kent, D. A. Leigh, J.-F. Lemonnier, Z. Li, C. A. Muryn, L. I. Palmer, Y. Song, G. F. S. Whitehead, R. J. Young, *Nature* **2020**, *588*, 429–435.

[9] S. D. P. Fielden, D. A. Leigh, S. L. Woltering, *Angew. Chem. Int. Ed.* **2017**, *56*, 11166–11194; *Angew. Chem.* **2017**, *129*, 11318–11347.

[10] a) G. Christou, D. Gatteschi, D. N. Hendrickson, R. Sessoli, *MRS Bull.* **2000**, *25*, 66–71; b) D. Gatteschi, R. Sessoli, J. Villain, *Molecular Nanomagnets*, Oxford University Press, Oxford, **2006**.

[11] a) R. Sessoli, D. Gatteschi, A. Caneschi, M. A. Novak, *Nature* **1993**, *365*, 141–143; b) T. Lis, *Acta Crystallogr. Sect. B* **1980**, *36*, 2042–2046; c) S. M. J. Aubin, M. W. Wemple, D. M. Adams, H.-L. Tsai, G. Christou, D. N. Hendrickson, *J. Am. Chem. Soc.* **1996**, *118*, 7746–7754.

[12] a) L. Bogani, W. Wernsdorfer, *Nat. Mater.* **2008**, *7*, 179–201; b) J. Lehmann, A. Gaita-Arino, E. Coronado, D. Loss, *J. Mater. Chem.* **2009**, *19*, 1672–1677; c) J. Camarero, E. Coronado, *J. Mater. Chem.* **2009**, *19*, 1678–1684; d) K. Katoh, H. Isshiki, T. Komeda, M. Yamashita, *Coord. Chem. Rev.* **2011**, *255*, 2124–2148.

[13] a) D. Woodruff, R. E. P. Winpenny, R. A. Layfield, *Chem. Rev.* **2013**, *113*, 5110–5148; b) J. D. Rinehart, J. R. Long, *Chem. Sci.* **2011**, *2*, 2078–2085; c) R. Sessoli, A. K. Powell, *Coord. Chem. Rev.* **2009**, *253*, 2328–2341.

[14] a) J. M. Frost, K. L. M. Harriman, M. Murugesu, *Chem. Sci.* **2016**, *7*, 2470–2491; b) D. Maniaki, E. Pilichos, S. P. Perlepes, *Front. Chem.* **2018**, *6*, 461; c) G. A. Craig, M. Murrie, *Chem. Soc. Rev.* **2015**, *44*, 2135–2147.

[15] a) V. V. Novikov, A. A. Pavlov, Y. V. Nelyubina, M.-E. Boulon, O. A. Varzatskii, Y. Z. Voloshin, R. E. P. Winpenny, *J. Am. Chem. Soc.* **2015**, *137*, 9792–9795; b) M. Murrie, *Chem. Soc. Rev.* **2010**, *39*, 1986–1995; c) A. K. Bar, C. Pichon, J.-P. Sutter, *Coord. Chem. Rev.* **2016**, *308*, 346–380; d) K. Chakarawet, P. C. Bunting, J. R. Long, *J. Am. Chem. Soc.* **2018**, *140*, 2058–2061; e) M. A. Hay, C. J. McMonagle, C. Wilson, M. R. Probert, M. Murrie, *Inorg. Chem.* **2019**, *58*, 9691–9697.

[16] a) C.-F. Lee, D. A. Leigh, R. G. Pritchard, D. Schultz, S. J. Teat, G. A. Timco, R. E. P. Winpenny, *Nature* **2009**, *458*, 314–318; b) A. Fernandez, J. Ferrando-Soria, E. M. Pineda, F. Tuna, I. J. Vitorica-Yrezabal, C. Knappke, J. Ujma, C. A. Muryn, G. A. Timco, P. E. Barran, A. Ardavan, R. E. P. Winpenny, *Nat. Commun.* **2016**, *7*, 10240.

[17] A. Fernandez, E. Moreno Pineda, J. Ferrando-Soria, E. J. L. McInnes, G. A. Timco, R. E. P. Winpenny, *Chem. Commun.* **2015**, *51*, 11126–11129.

[18] J. Ferrando-Soria, A. Fernandez, I. J. Vitorica-Yrezabal, D. Asthana, C. A. Muryn, F. Tuna, G. A. Timco, R. E. P. Winpenny, *Chem. Commun.* **2019**, *55*, 2960–2963.

[19] M. Cirulli, E. Salvadori, Z.-H. Zhang, M. Dommett, F. Tuna, H. Bamberger, J. E. M. Lewis, A. Kaur, G. J. Tizzard, J. van Slageren, R. Crespo-Otero, S. M. Goldup, M. M. Roessler, *Angew. Chem. Int. Ed.* **2021**, *60*, 16051–16058; *Angew. Chem.* **2021**, *133*, 16187–16194.

[20] F. Weldon, L. Hammarström, E. Mukhtar, R. Hage, E. Gunneweg, J. G. Haasnoot, J. Reedijk, W. R. Browne, A. L. Guckian, J. G. Vos, *Inorg. Chem.* **2004**, *43*, 4471–4481.

[21] a) M. Marchivie, P. Guionneau, J.-F. Létard, D. Chasseau, *Acta Crystallogr. Sect. B* **2003**, *59*, 479–486; b) I. Krivokapic, M. Zerara, M. L. Daku, A. Vargas, C. Enachescu, C. Ambrus, P. Tregenna-Piggott, N. Amstutz, E. Krausz, A. Hauser, *Coord. Chem. Rev.* **2007**, *251*, 364–378.

[22] T. K. Ronson, D. A. Roberts, S. P. Black, J. R. Nitschke, *J. Am. Chem. Soc.* **2015**, *137*, 14502–14512.

[23] K. S. Cole, R. H. Cole, *J. Chem. Phys.* **1941**, *9*, 341–351.

[24] D. Reta, N. F. Chilton, *Phys. Chem. Chem. Phys.* **2019**, *21*, 23567–23575.

[25] J. H. Van Vleck, *Phys. Rev.* **1940**, *57*, 426–447.

[26] K. N. Shrivastava, *Phys. Status Solidi A* **1983**, *117*, 437–458.

Supporting Information

Self-assembly synthesis of a [2]catenane Co(II) single-molecule magnet

Benjamin H. Wilson, Jas S. Ward, David C. Young, Jun-Liang Liu, Corine Mathonière, Rodolphe Clérac* and Paul E. Kruger**

General Information

All starting materials and reagents were reagent grade and used as received from standard suppliers. Solvents were HPLC grade and used as received. ^{1}H and ^{13}C NMR measurements were performed using an Agilent 400 NMR spectrometer operating at 400 MHz for ^{1}H and 101 MHz for ^{13}C. Chemical shift values are given in parts per million (PPM) and spectra were referenced to residual solvent peaks. A Bruker ALPHA Platinum ATR FT-IR spectrometer was used to measure samples in the range 4000-400 cm^{-1}. The following abbreviations were used to describe the signals: s (strong), m (medium), w (weak), br (broad). Melting points were recorded on an Electrothermal melting point apparatus and are uncorrected. Mass spectrometry was performed using a Bruker maXis 4G time of flight spectrometer operating in ESMS+ mode with values are given as MH^{+}.

Syntheses

Synthesis of L

Synthesis of 2-Pyridylamidrazone

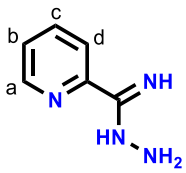

2-Pyridylamidrazone was synthesized following the literature preparation of Weldon *et al.*[S1] M.pt. 85°C, Lit. 95°C. δ_H (400 MHz, $CDCl_3$): 8.50 (1H, d, J = 4.7 Hz, H_a), 7.99 (1H, d, J = 7.8 Hz, H_d), 7.67 (1H, dt, J = 7.8, 1.8 Hz, H_c), 7.21 - 7.29 (1H, m, H_b), 5.26 (3H, br. s, H_{NH}).

Synthesis of N,N'-terephthaloyl-bis(2-pyridyl)hydrazidine

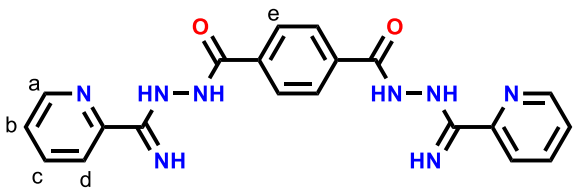

N,N'-Terephthaloyl-bis((2-pyridyl)hydrazidine was synthesised following the literature preparation of Weldon *et al.*[S1] M.pt. >360°C, Lit. >300°C. ^{1}H-NMR (400 MHz, [D_6]-DMSO) δ = 10.32 (1H, s, H_{NH}), 8.60 (1H, d, J = 3.5 Hz, H_a), 8.19 (2H, d, J = 7.8 Hz, H_c), 7.98 (4H, s, H_e), 7.86 - 7.95 (2H, m, H_b), 7.45 - 7.52 (1H, m, H_d). ^{13}C-NMR (101 MHz, [D_6]-DMSO) δ = 163.0, 150.0, 148.6, 137.4, 127.9, 125.3, 121.2. ESI-MS: $[C_{20}H_{19}N_8O_2]^{+}$ meas. 403.1628 calc. 403.1625. $\bar{\nu}_{max}$ / cm^{-1}: 3413 (m), 3288 (w), 3166 (br, m), 1623 (s), 1586 (s), 1564 (w), 1532 (s), 1504 (w), 1471 (s), 1442 (m), 1392 (w), 1313 (s), 1279 (w), 1157 (w), 1130 (w), 1047 (w), 1016 (s).

*Synthesis of 1,2-bis(5-(2-pyridyl)-4H-1,2,4-triazol-3-yl)benzene (**H_2L**)*

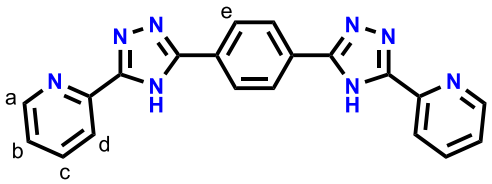

1,2-bis(5-(2-pyridyl)-4H-1,2,4-triazol-3-yl)benzene (**H_2L**) was synthesised following the literature preparation of Weldon *et al.*[S1] M.pt. >360°C, Lit. >300°C. ^{1}H-NMR (400 MHz, [D$_6$]-DMSO) δ = 8.72 (2H, d, J = 3.9 Hz, H$_a$), 8.16 - 8.24 (6H, m, H$_d$ and H$_e$), 8.01 (2H, t, J = 7.6 Hz, H$_c$), 7.49 - 7.57 (2H, m, H$_b$). ^{13}C-NMR (101 MHz, [D$_6$]-DMSO) δ = 150.8, 150.1, 138.2, 127.8, 127.0, 125.4, 123.6, 121.9. ESI-MS: $[C_{20}H_{15}N_8]^+$ meas. 367.1393 calc. 367.1414. $\bar{\nu}_{max}$ / cm^{-1}: 3182 (br, m), 1596 (w), 1478 (s), 1463 (w), 1414 (s), 1142 (s), 1103 (w), 1007 (s).

Synthesis of $[Co_4(H_2L)_6]_2(ClO_4)_7Br_9$, 1

A nitromethane (30 mL) suspension of **H_2L** (55 mg, 0.15 mmol) and $Co(ClO_4)_2$•$6H_2O$ (37 mg, 0.10 mmol) was stirred at 50°C for several hours to give an orange solution. An aqueous solution of LiBr in H_2O (0.125 mol L^{-1}, 600 µL, 0.075 mmol) was added and the reaction stirred at 50°C for a further 1.5 hours. The cooled solution was filtered to give a clear orange filtrate. Vapour diffusion of chloroform into the nitromethane solution over two days at ambient temperature yielded orange blocks suitable for single crystal X-ray diffraction. Recovered yield = 13 mg (0.002 mmol, 2%). $\bar{\nu}_{max}$ / cm^{-1}: 2917 (w), 2849 (w), 1615 (m), 1585 (w), 1568 (w), 1464 (m), 1409 (br, m), 1287 (w), 1003 (s), 984 (br, s). Elemental: found C, 43.2 H, 3.02 N, 19.46%; $[Co_4(C_{20}H_{14}N_8)_6]_2(ClO_4)_7Br_9 \cdot 4CHCl_3 \cdot 2H_2O$ requires C, 43.1 H, 2.61 N, 19.8%. ESI-MS: $[(Co_4(C_{20}H_{14}N_8)_6)\text{-}5H]^{3+}$ meas. 809.5178 calc. 809.4998 $[(Co_4(C_{20}H_{14}N_8)_6)_2\text{-}10H]^{6+}$ meas. 809.5178 calc. 809.4999 (See Figure S1).

Synthesis of $[Co_4(H_2L)_6]Br_4(ClO_4)_4$, 2

A nitromethane (30 mL) suspension of **H_2L** (55 mg, 0.15 mmol) and $Co(ClO_4)_2.6H_2O$ (37 mg, 0.10 mmol) was stirred at 50°C for 1 hour to give an orange solution. An aqueous solution of LiBr in H_2O (0.125 mol L^{-1}, 600 µL, 0.075 mmol) was added and stirred at 60°C for a further 4 hours. The cooled solution was filtered to give a clear orange filtrate. Vapor diffusion of chloroform into the nitromethane spiked with 50 µL m-xylene over three days at ambient temperature yielded orange blocks suitable for single crystal X-ray diffraction, which corresponded to **1**. After several weeks, orange flake crystals suitable for single crystal X-ray diffraction grew on top of the blocks corresponding to **2**. These crystals were only obtained in trace amounts and therefore no analysis other than single crystal X-ray diffraction was carried out.

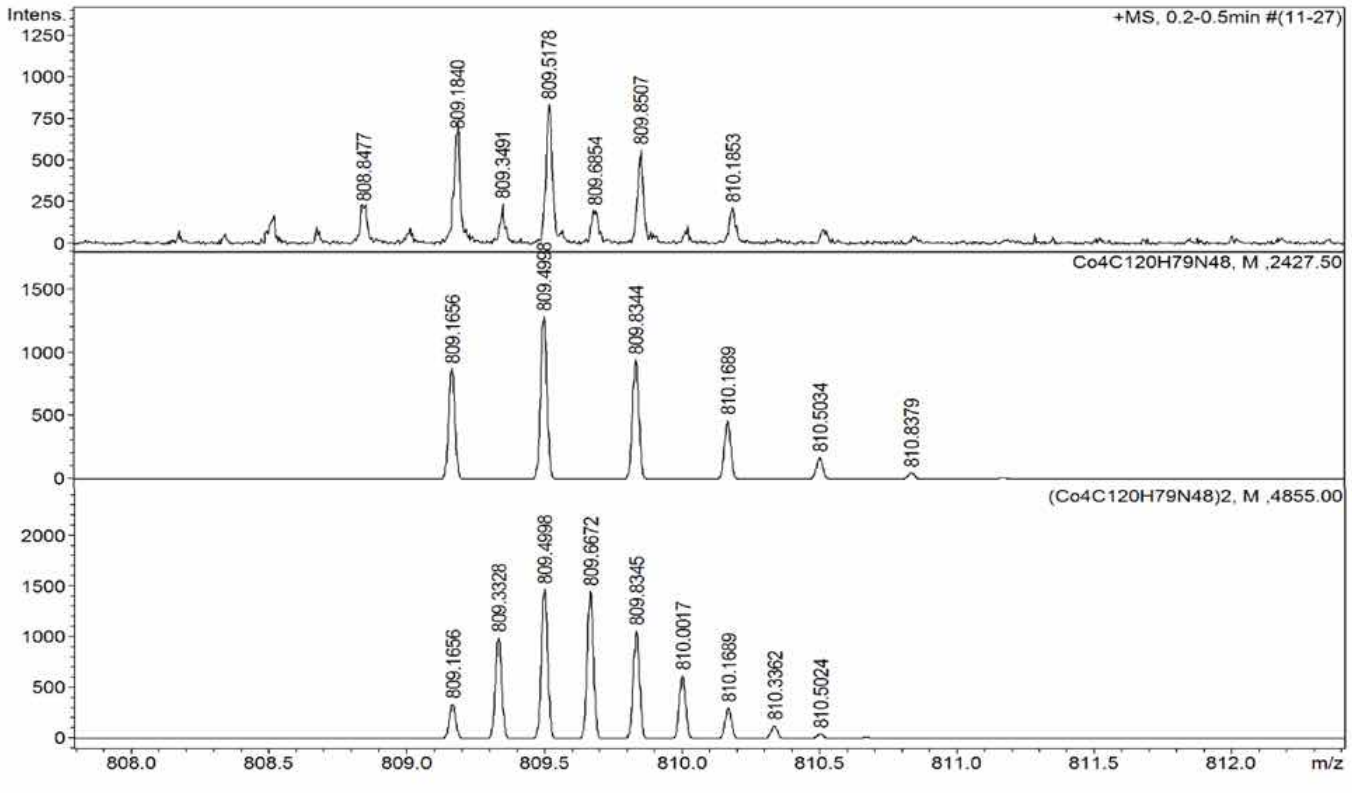

Figure S1. HR-ESI Mass spectrum of **1** corresponding to $\{(Co_4(\mathbf{H_2L})_6)\text{-}5H\}^{3+}$ (non-catenated structure) and $\{(Co_8(\mathbf{H_2L})_{12})\text{-}10H\}^{6+}$ (catenated structure). The top spectrum is the experimentally measured while the middle is the calculated spectrum for the non-catenated structure and the bottom is the calculated spectrum for the catenated structure. The rectangle and catenane peaks overlap to produce a superimposed set of peaks that are observed experimentally.

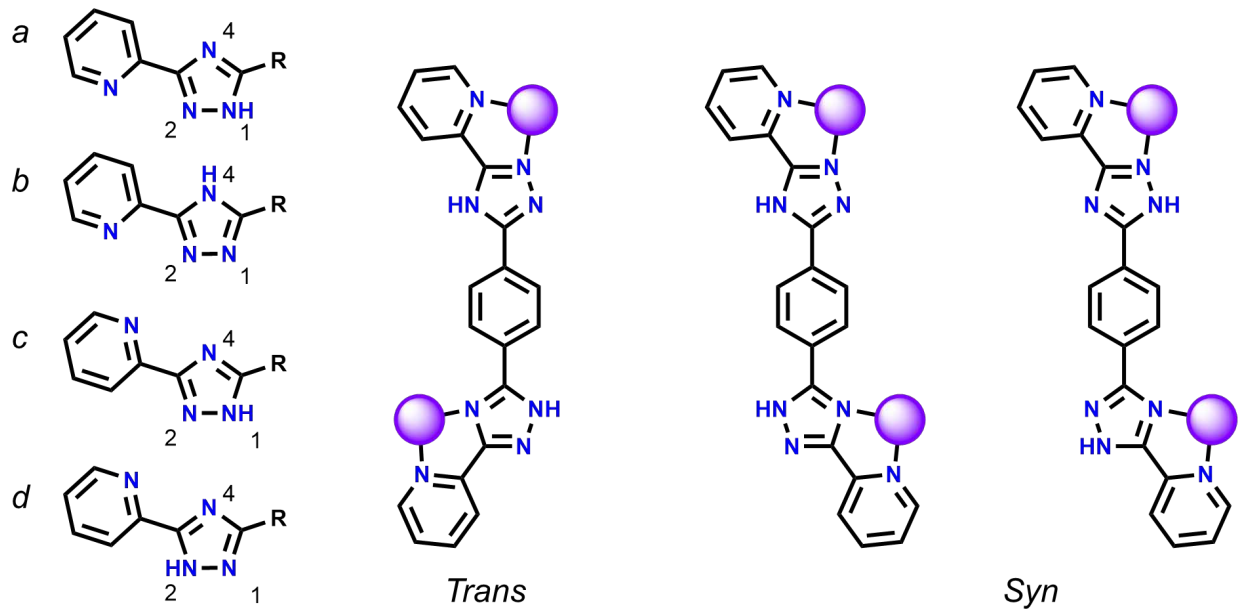

Figure S2. (Left) Numbering scheme of the 3-pyridyl-1,2,4-triazole ligands used in the following discussion. Four possible tautomers can occur, two of which facilitate chelation of the metal center via the pyridyl nitrogen and N-2 of the triazole (*a* and *b*) while two facilitate chelation of the metal center via the pyridyl nitrogen and N-4 of the triazole (*c* and *d*). (Middle) The *trans*- conformation of the ligand with the two bidentate binding regions orientated in opposite directions as it occurs in **1** featuring tautomers *b* and *c*. (Right) The two *syn*- conformation of the ligand with the two bidentate binding regions orientated in the same directions as they occur in **1** for which one features tautomers *b* and *c* and the other *a* and *d*.

X-Ray Crystallography

General Information

The structural analysis at 120 K was performed on an Agilent dual wavelength SuperNova with monochromated Cu-Kα (λ = 1.54178 Å) or Mo-Kα (λ = 0.70926 Å) radiation. CrysAlisPro was used for the data collection and data processing.[S2] The structure was solved using intrinsic phasing with SHELXT[S3] and refined on Olex2[S4] using all data by full matrix least-squares procedures with SHELXL.[S5] Multi-scan absorption correction using SCALE3 ABSPACK.[S6] Hydrogen atoms were included in calculated positions with isotropic displacement parameters 1.2 times the isotropic equivalent of their carrier atoms. For both **1** and **2**, no sensible disorder model could be found for the large number of solvent molecules present in each structure. Therefore, the SQUEEZE[S7] function of PLATON[S8] was applied. Structures were deposited in the Cambridge Structure Database (CCDC 2098246-2098247).

Table S1. Crystallographic data for **1** and **2**

Identification code	**1**	**2**
Empirical formula	$C_{240}H_{168}Br_9Cl_7Co_8N_{96}O_{28}$	$C_{122}H_{90}Br_4Cl_4Co_4N_{50}O_{20}$
Formula weight	6283.47	3273.59
Temperature /K	120.04(10)	120.01(10)
Crystal system	tetragonal	monoclinic
Space group	$I4_1/a$	$P2_1/c$
a /Å	33.6515(12)	21.0336(7)
b /Å	33.6515(12)	49.0215(12)
c /Å	31.4034(13)	18.0219(4)
α /°	90	90
β /°	90	98.838(3)
γ /°	90	90
Volume /Å^3	35562(3)	18361.7(8)
Z	4	4
ρ_{calc} g/cm^3	1.174	1.184
μ /mm^{-1}	1.490	4.869
F(000)	12616.0	6592.0
Crystal size /mm^3	0.1649 × 0.1181 × 0.0885	0.3362 × 0.2141 × 0.0798
Radiation	MoKα (λ = 0.71073 Å)	CuKα (λ = 1.54184 Å)
2Θ range for data collection /°	5.156 to 50.054	7.018 to 103.034
Index ranges	$-40 \le h \le 24$, $-27 \le k \le 40$, $-23 \le l \le 37$	$-21 \le h \le 20$, $-37 \le k \le 49$, $-16 \le l \le 18$
Reflections collected	50991	74820
Independent reflections	15610 [R_{int} = 0.1084, R_{sigma} = 0.1608]	19848 [R_{int} = 0.0930, R_{sigma} = 0.1277]
Data/restraints/parameters	15610/528/844	19848/311/1851
Goodness-of-fit on F^2	1.249	1.459
Final R indexes [$I \ge 2\sigma(I)$]	R_1 = 0.1788, wR_2 = 0.4293	R_1 = 0.1667, wR_2 = 0.4191
Final R indexes [all data]	R_1 = 0.3138, wR_2 = 0.5128	R_1 = 0.2287, wR_2 = 0.4640
Largest diff. peak/hole / e Å^{-3}	1.99/-0.96	2.42/-1.21

Specific Refinement Details

*$[Co_4(\mathbf{H_2L})_4]_2Br_9[ClO_4]_7$ (**1**)*

The single crystals employed immediately began to desolvate after removal from the mother liquor. Swift (<15 sec) handling prior to quenching in the cryostream was required to collect good quality data. The high-resolution data was observed to rapidly fall off, an expected consequence of the supramolecular nature of **1** and the large amount of void space it possessed. Therefore, the completeness of the outer data was less than ideal. Nevertheless, the quality of the data is more than sufficient to establish the identity of the structure. The asymmetric unit contained a quarter of a molecule of the $[Co_4(\mathbf{H_2L})_6]_2$ complex. The bromide and perchlorate anions were found to be disordered with partial occupancies over multiple positions, with the perchlorates requiring thermal parameter restraints to sensibly model. Several AFIX constraints, in conjunction with thermal parameter restraints, were necessary to model the heterocycles in the framework. Due to the rapid desolvation of the complex, the highly disordered solvates could not be adequately identified or modelled and the electron density of which were accounted for using the SQUEEZE routine in PLATON, where the program identified solvent accessible voids totalling 9786.5 Å^3 and 3116.4 electrons per unit cell were recovered.

*$[Co_4(\mathbf{H_2L})_4]Br_4[ClO_4]_4^{2+}$ (**2**)*

Much like **1**, the single crystals employed immediately began to desolvate after removal from the mother liquor. Swift (<15 sec) handling prior to quenching in the cryostream was required to collect good quality data. The high-resolution data was observed to rapidly fall off, an expected consequence of the supramolecular nature of **2** and the large amount of void space it possessed, therefore the completeness of the outer data was less than ideal. Nevertheless, the quality of the data is more than sufficient to establish the identity of the structure. The asymmetric unit contained one molecule of the $[Co_4(\mathbf{H_2L})_6]$ complex. The bromide and perchlorate anions were found to be disordered with partial occupancies over multiple positions, with the perchlorates requiring thermal parameter restraints (and in two instances, thermal parameter constraints) to sensibly model. The bond lengths about Co1 and Co3 indicate that they are Co^{3+} while Co2 and Co4 are Co^{2+}. Due to the large void space resulting in significant disorder of the anions and solvent molecules, the remaining two anions cannot be accurately located and were therefore not modelled. To successfully model the heterocycles of the framework, thermal parameter restraints were applied. The highly disordered solvates could not be adequately identified or modelled and the electron density of which were accounted for using the SQUEEZE routine in PLATON, where the program identified solvent accessible voids totalling 5128.4 Å^3 and 1994.7 electrons per unit cell were recovered.

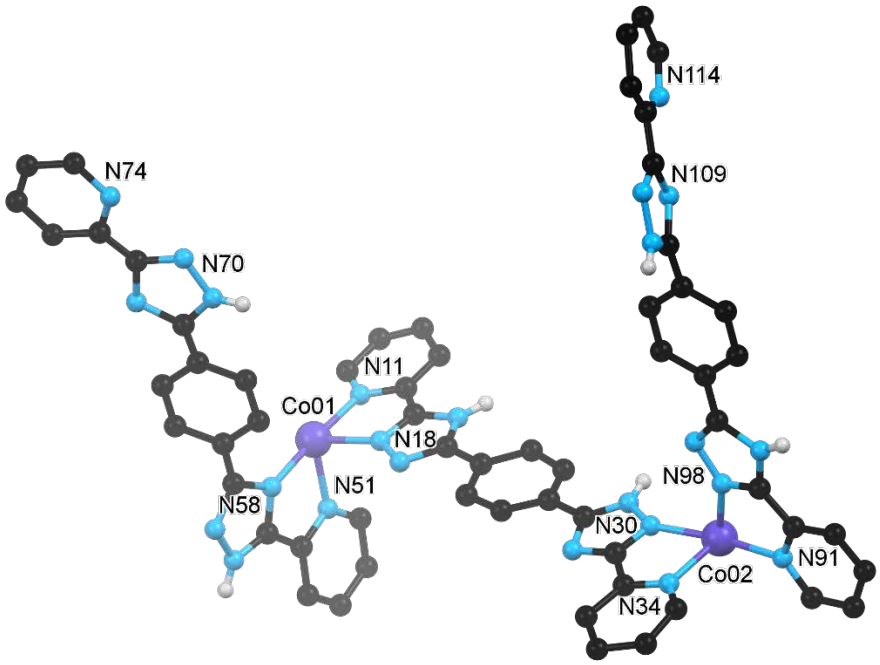

Figure S3. Asymmetric unit of **1** with nitrogen donor atoms and the two crystallographically unique Co(II) centres labelled. Hydrogen atoms, solvent molecules and anions are omitted for clarity.

Table S2. Crystallographic Co-N bond lengths and *cis*- N-Co-N angles for **1** for the two crystallographically unique Co(II) centres at 120 K. The octahedral distortion parameter (Σ) is calculated from the sum of the deviation of the 12 *cis*- N-Co-N bond angles from 90°.[S9]

Co01						
Atoms	Distance (Å)	Atoms	Angle (°)	Atoms	Angle (°)	Σ
Co01-N11	2.11(1)	N11-Co01-N18	77.0(4)	N58-Co01-N70	94.5(4)	82.1
Co01-N18	2.09(1)	N18-Co01-N58	99.0(4)	N70-Co01-N11	87.7(3)	
Co01-N51	2.11(1)	N58-Co01-N74	88.4(4)	N18-Co01-N51	92.4(4)	
Co01-N58	2.14(1)	N74-Co01-N11	95.5(4)	N51-Co01-N74	90.3(4)	
Co01-N70	2.064(7)	N11-Co01-N51	99.5(4)	N74-Co01-N70	77.5(3)	
Co01-N74	2.191(6)	N51-Co01-N58	79.0(4)	N70-Co01-N18	100.5(3)	
Co02						
Atoms	Distance (Å)	Atoms	Angle (°)	Atoms	Angle (°)	Σ
Co02-N30	2.13(1)	N30-Co02-N34	75.9(4)	N91-Co02-N114	93.4(5)	82.7
Co02-N34	2.14(1)	N34-Co02-N91	94.2(4)	N114-Co02-N30	88.3(4)	
Co02-N91	2.17(1)	N91-Co02-N109	94.7(4)	N34-Co02-N98	93.6(4)	
Co02-N98	2.09(1)	N109-Co02-N30	95.2(4)	N98-Co02-N109	94.7(4)	
Co02-N109	2.047(9)	N30-Co02-N98	103.6(4)	N109-Co02-N114	80.0(4)	
Co02-N114	2.19(1)	N98-Co02-N91	75.6(4)	N114-Co02-N34	93.1(4)	

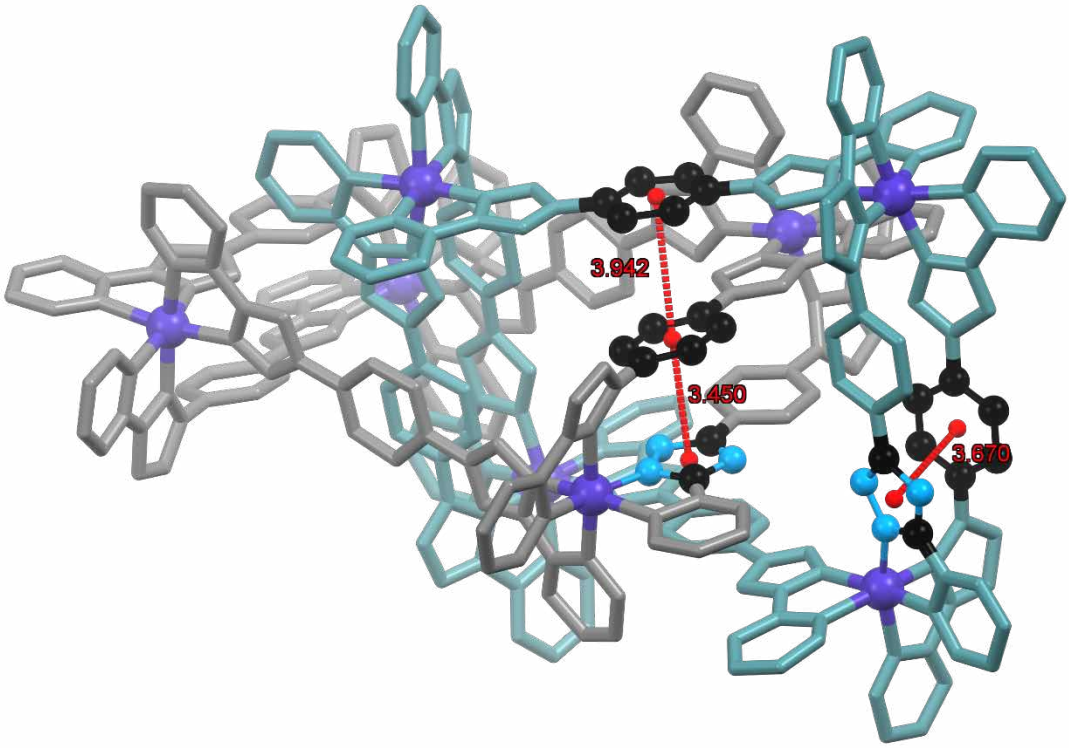

Figure S4. π-π stacking interactions for **1** occurring between the triazole and phenyl rings. The π(centroid) shown as red spheres and the π(centroid)⋯ π(centroid) separations are shown in red. Hydrogen atoms, solvent molecules and anions are omitted for clarity.

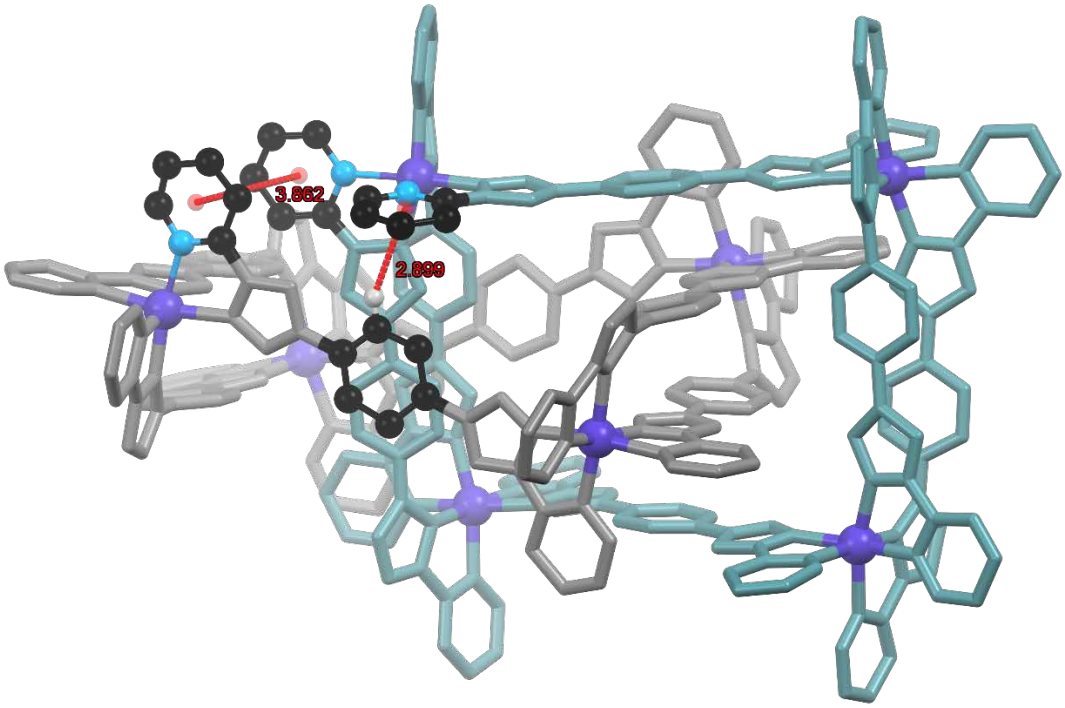

Figure S5. π-π stacking and C-H⋯π interactions occurring between the phenyl and pyridine rings of the interlinked squares π(centroid) shown as red spheres and the π(centroid)⋯π(centroid) separation are shown in red. Hydrogen atoms not participating in the illustrated interactions, solvent molecules and anions are omitted for clarity.

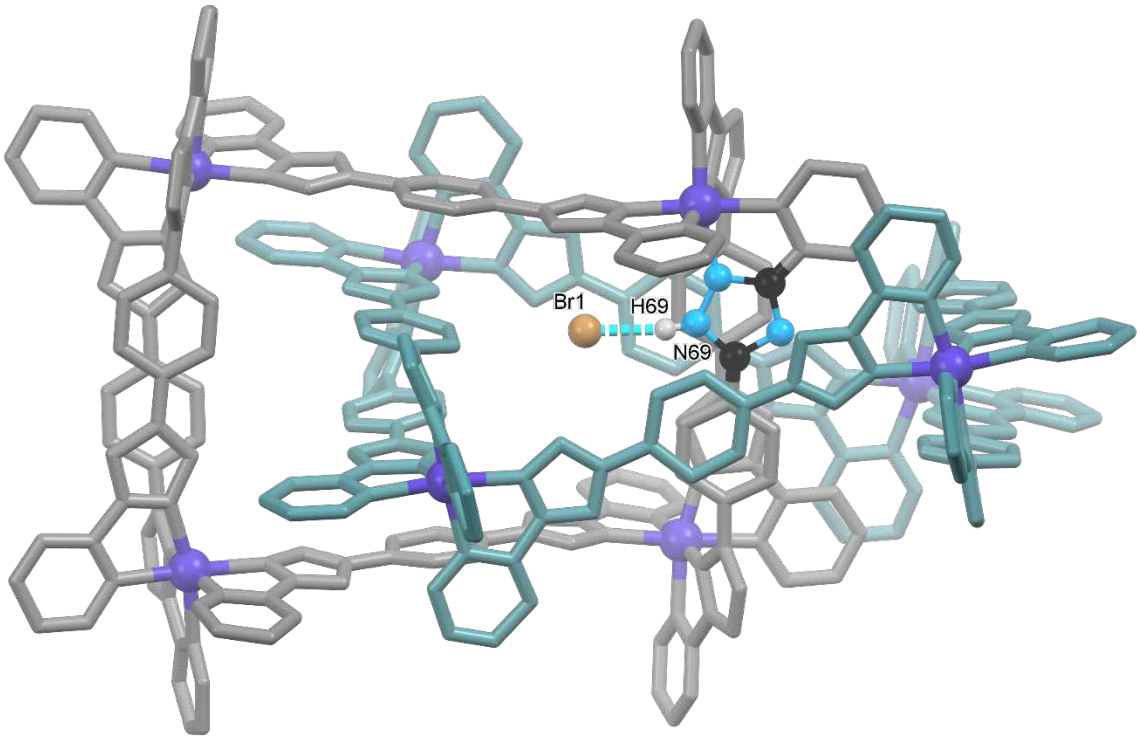

Figure S6. Hydrogen bonding interaction for **1** between the N-H triazole moiety and one of the bromide anions occupying the cavity of the catenane (the H···Br separation is shown in pale blue). Hydrogen atoms, solvent molecules and anions not participating in the illustrated hydrogen bonding interactions are omitted for clarity.

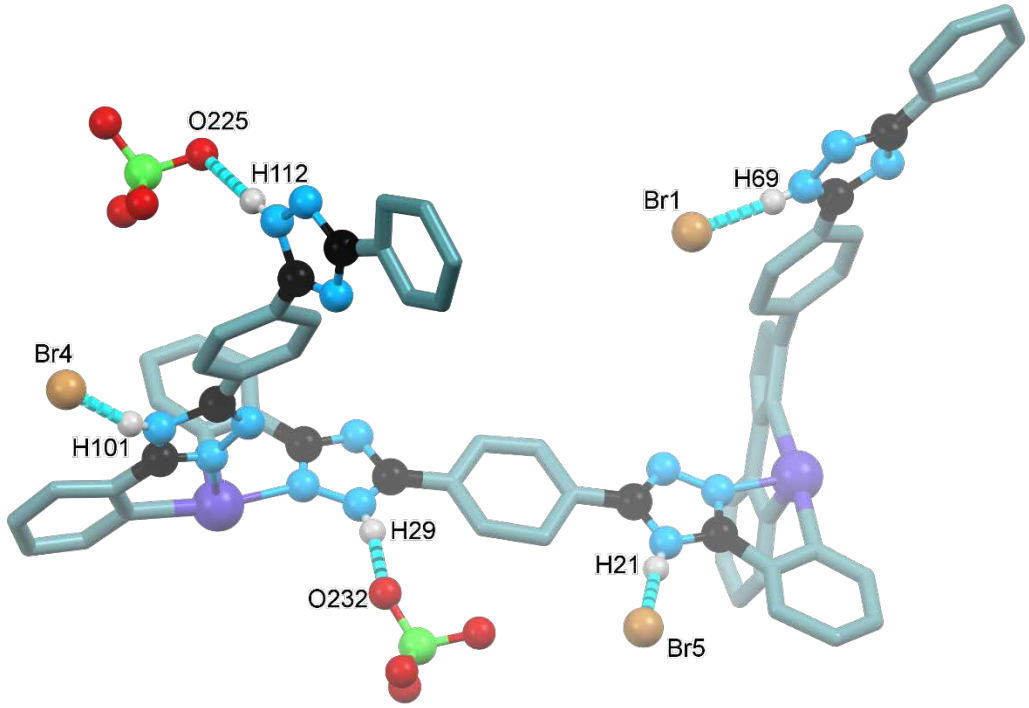

Figure S7. Hydrogen bonding interactions of the N-H moieties of the triazole rings with bromide and perchlorate anions in **1** (H···A separations are shown in blue). Hydrogen atoms, solvent molecules and anions not participating in the illustrated interactions are omitted for clarity.

Table S3. Hydrogen bonding parameters for **1**.

D-H···A	d(D-H) Å	d(D-H···A) Å	d(D···A) Å	<(D-H···A) °	Symmetry Code
N21-H21···Br5	0.86(1)	1.98(2)	2.84(2)	172.7(8)	*x*, *y*, *z*
N29-H29···O232	0.86(1)	1.79(2)	2.64(2)	168.9(8)	*x*, *y*, *z*
N69-H69···Br1	0.859(6)	2.178(4)	3.026(7)	169.5(5)	1.25-*y*, 1/4+*x*, 1.25-*z*
N101-H101···Br4	0.86(1)	1.88(2)	2.70(3)	160(1)	*x*, *y*, *z*
N112-H112···O225	0.860(1)	2.09(1)	2.94(1)	171.5(7)	-1/4, 1.75-*x*, -1/4+*z*

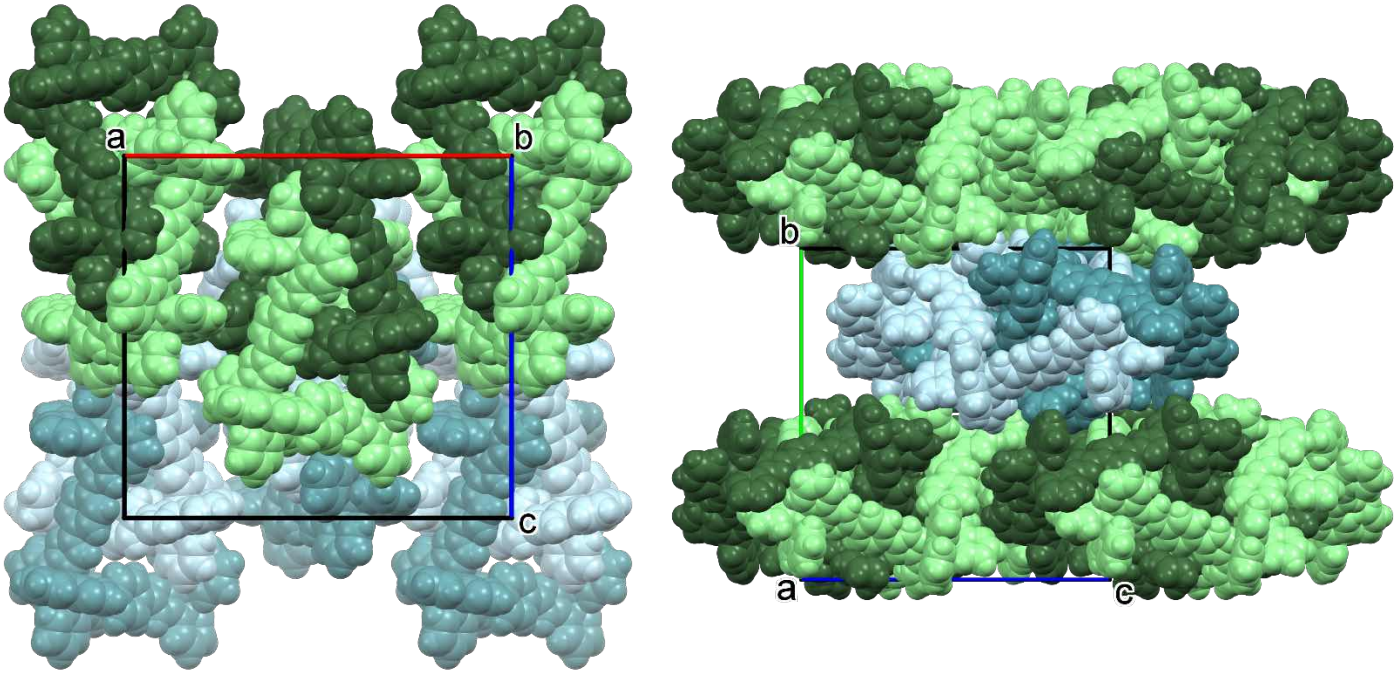

Figure S8. Crystal packing for **1**. (Left) The off-set packing of the catenane units parallel to the crystallographic *b*-axis (red). Complexes out of the plane are shown in green while complexes into the plane are shown in blue for clarity. (Right) The end-on-end packing of the catenane units in a one-dimensional arrangement parallel to the crystallographic *c*-axis. The supramolecular chains are made up of catenanes shown in either green or blue.

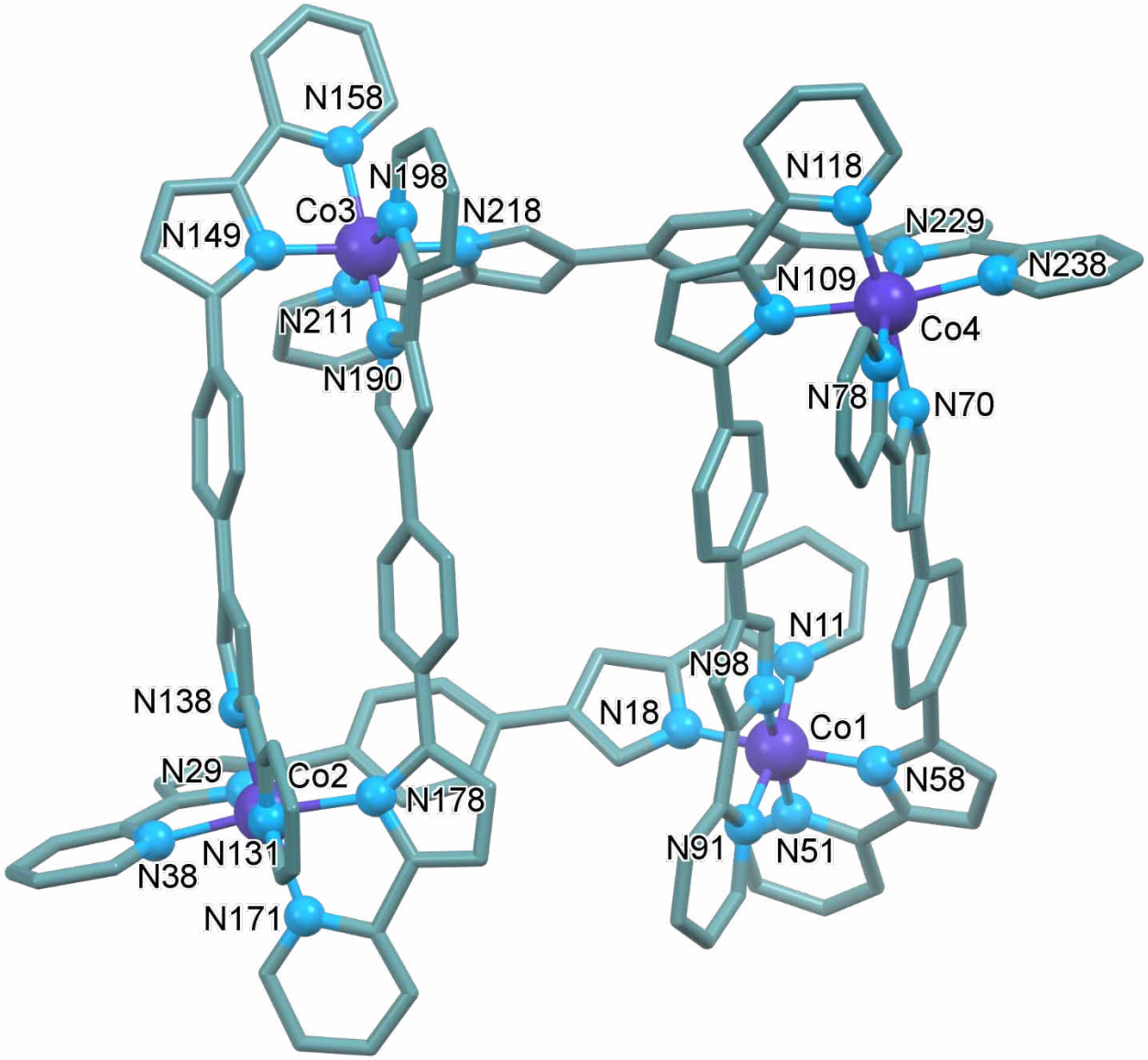

Figure S9. Asymmetric unit of **2** with labelled nitrogen donor atoms and the four crystallographically unique Co(II) centres. Hydrogen atoms, solvent molecules and anions are omitted for clarity.

Table S4. Crystallographic Co-N bond lengths and *cis*- N-Co-N angles for the four crystallographically unique Co(II) centres at 120 K in **2**. The octahedral distortion parameter (Σ) is calculated from the sum of the deviation of the 12 *cis*- N-Co-N bond angles from 90°.[S9]

			Co1			
Atoms	Distance (Å)	Atoms	Angle (°)	Atoms	Angle (°)	Σ
Co1-N11	1.97(1)	N11-Co1-N18	81.3(5)	N91-Co1-N98	82.1(5)	51.4
Co1-N18	1.88(1)	N18-Co1-N91	90.1(5)	N98-Co1-N11	90.9(5)	
Co1-N51	1.97(1)	N91-Co1-N58	94.9(5)	N18-Co1-N51	94.1(5)	
Co1-N58	1.93(1)	N58-Co1-N11	93.9(5)	N51-Co1-N58	83.2(5)	
Co1-N91	1.94(1)	N11-Co1-N51	93.6(5)	N58-Co1-N98	94.9(5)	
Co1-N98	1.89(1)	N51-Co1-N91	93.7(5)	N98-Co1-N18	88.1(5)	
			Co2			
Atoms	Distance (Å)	Atoms	Angle (°)	Atoms	Angle (°)	Σ
Co2-N29	2.15(1)	N29-Co2-N38	77.6(5)	N131-Co2-N171	92.7(5)	92.4
Co2-N38	2.16(1)	N38-Co2-N131	95.7(5)	N171-Co2-N29	96.5(5)	
Co2-N131	2.14(1)	N131-Co2-N178	82.2(5)	N38-Co2-N138	91.7(5)	
Co2-N138	2.13(1)	N178-Co2-N29	105.4(5)	N138-Co2-N178	93.6(5)	
Co2-N171	2.09(1)	N29-Co2-N138	95.7(5)	N178-Co2-N171	78.8(5)	
Co2-N178	2.11(1)	N138-Co2-N131	75.6(5)	N171-Co2-N38	95.3(5)	
			Co3			
Atoms	Distance (Å)	Atoms	Angle (°)	Atoms	Angle (°)	Σ
Co3-N149	1.96(1)	N149-Co3-N158	82.7(6)	N218-Co3-N211	80.0(7)	58.5
Co3-N158	2.03(2)	N158-Co3-N218	95.5(6)	N211-Co3-N149	95.9(6)	
Co3-N190	1.88(1)	N218-Co3-N190	87.3(6)	N158-Co3-N198	91.8(5)	
Co3-N198	1.97(1)	N190-Co3-N149	95.0(5)	N198-Co3-N190	81.3(5)	
Co3-N211	1.97(1)	N149-Co3-N198	93.3(5)	N19-co3-N211	93.0(6)	
Co3-N218	1.91(1)	N198-Co3-N218	91.0(5)	N211-Co3-N158	94.3(7)	
			Co4			
Atoms	Distance (Å)	Atoms	Angle (°)	Atoms	Angle (°)	Σ
Co4-N70	2.08(1)	N70-Co4-N78	75.9(5)	N118-Co4-N238	94.2(7)	94.5
Co4-N78	2.17(1)	N78-Co4-N118	91.5(5)	N238-Co4-N70	91.8(7)	
Co4-N109	2.10(1)	N118-Co4-N229	95.9(6)	N78-Co4-N109	84.1(5)	
Co4-N118	2.18(1)	N229-Co4-N70	97.1(6)	N109-Co4-N229	102.3(6)	
Co4-N229	2.10(2)	N70-Co4-N109	97.0(6)	N229-Co4-N238	76.3(7)	
Co4-N238	2.17(2)	N109-Co4-N118	77.3(6)	N238-Co4-N78	98.3(6)	

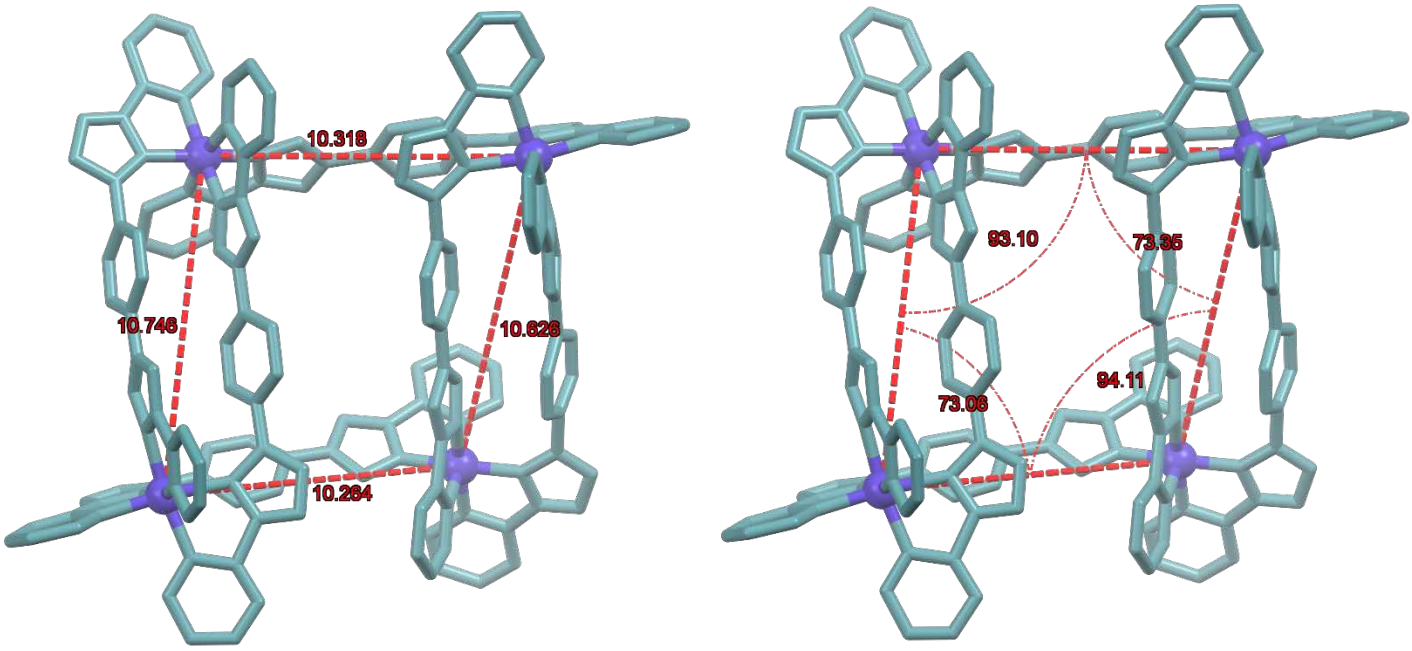

Figure S10. (Left) Co···Co separations (shown in red) and (Right) Co···Co···Co angles (shown in red) of the distorted square structure of **2**. Hydrogen atoms, solvent molecules and anions omitted for clarity.

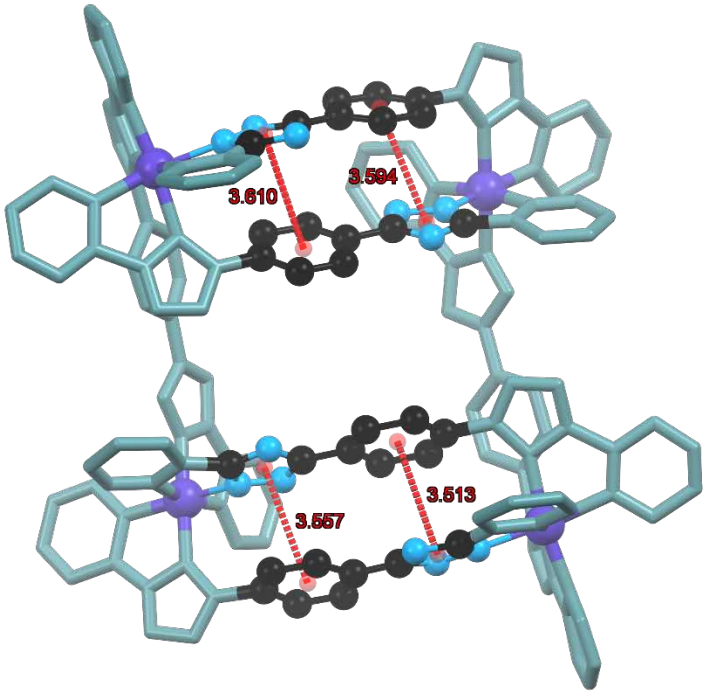

Figure S11. Four crystallographically unique π-π interactions between the triazole and phenyl rings for **2** with the π(centroid) shown as red spheres and the π(centroid)···π(centroid) separations shown in red.

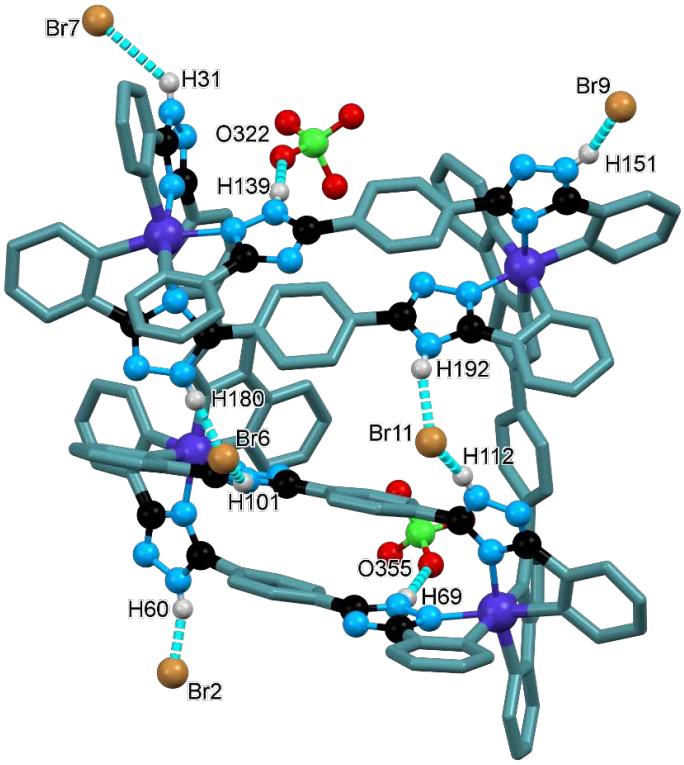

Figure S12. Hydrogen bonding interactions of the N-H moieties of the triazole rings with bromide and perchlorate anions in **2** (H···A separations are shown in blue). Hydrogen atoms, solvent molecules and anions not participating in the illustrated interactions are omitted for clarity.

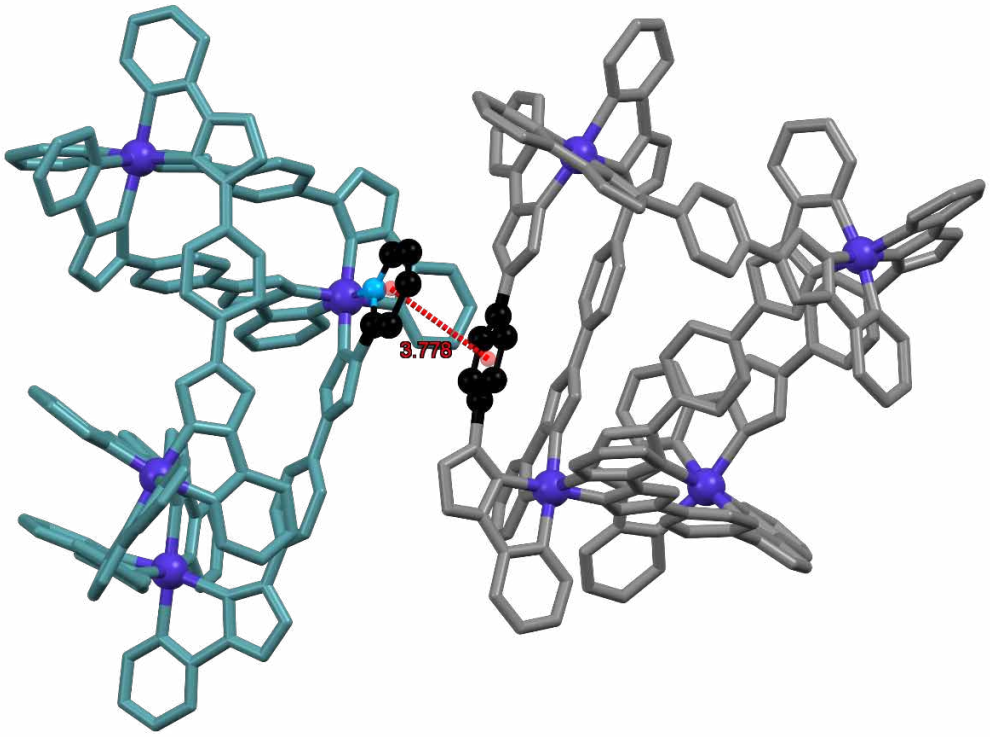

Figure S13. π-π interaction between the coordinated pyridine ring of one complex and the central phenyl spacer of another for **2** with the π(centroid) shown as red spheres and the π(centroid)···π(centroid) separation shown in red.

Table S5. Hydrogen bonding parameters for **2**.

D-H···A	d(D-H) Å	d(D-H···A) Å	d(D···A) Å	<(D-H···A) °	Symmetry Code
N31-H31···Br7	0.86(1)	2.81(2)	3.46(2)	134(1)	*x*, *y*, *z*
N60-H60···Br2	0.86(1)	1.88(1)	2.71(2)	162(1)	*x*, *y*, *z*
N101-H101···Br6	0.86(1)	2.04(1)	2.84(2)	154.6(8)	*x*, *y*, *z*
N112-H112···Br11	0.86(1)	1.88(1)	2.71(2)	162(1)	*x*, *y*, *z*
N139-H139···O322	0.86(1)	1.95(2)	2.80(2)	166.9(8)	*x*, *y*, *z*
N151-H151···Br9	0.86(2)	1.97(1)	2.77(2)	155(1)	*x*, *y*, *z*
N180-H180···Br6	0.86(1)	1.905(9)	2.77(2)	117(1)	*x*, *y*, *z*
N192-H192···Br11	0.86(1)	2.134(9)	2.83(2)	138(8)	*x*, *y*, *z*

Magnetic Measurements

General Information

Magnetic susceptibility measurements were performed on a Quantum Design SQUID MPMS-XL magnetometer and PPMS-9 susceptometer housed at the Centre de Recherche Paul Pascal at temperatures between 1.8 and 270 K and *dc* magnetic fields ranging from -7 to +7 T. The *ac* magnetic susceptibility measurements were performed in an oscillating *ac* field of 1 to 6 Oe with frequencies between 10 and 10000 Hz and various *dc* fields (including zero). The measurements were carried out on a freshly-filtered polycrystalline sample of **1** (10.75 mg) suspended in mineral oil and introduced in a sealed polyethylene bag (3 × 0.5 × 0.02 cm; 21.22 mg). A second polycrystalline sample of **1** (13.28 mg) covered and restrained in a minimum amount of frozen mother liquor within a sealed straw, was also measured for comparison. No evaporation of the mother liquor was observed during the measurement. The mass of the sample was estimated at 13.28 mg after the measurements and after the mother liquor removal/evaporation in air. The measurements on these two samples were found to be virtually identical and thus the extended set of data collected for the freshly-filtered polycrystalline sample are shown in this manuscript. Prior to the experiments, the field-dependent magnetization was measured at 100 K on each sample to exclude the presence of bulk ferromagnetic impurities. In fact, paramagnetic or diamagnetic materials should exhibit a perfectly linear dependence of the magnetization that extrapolates to zero at zero *dc* field; the samples appeared to be free of any ferromagnetic impurities. The magnetic susceptibilities were corrected for the sample holder, the mineral oil and the intrinsic diamagnetic contributions.

DC Magnetic Data

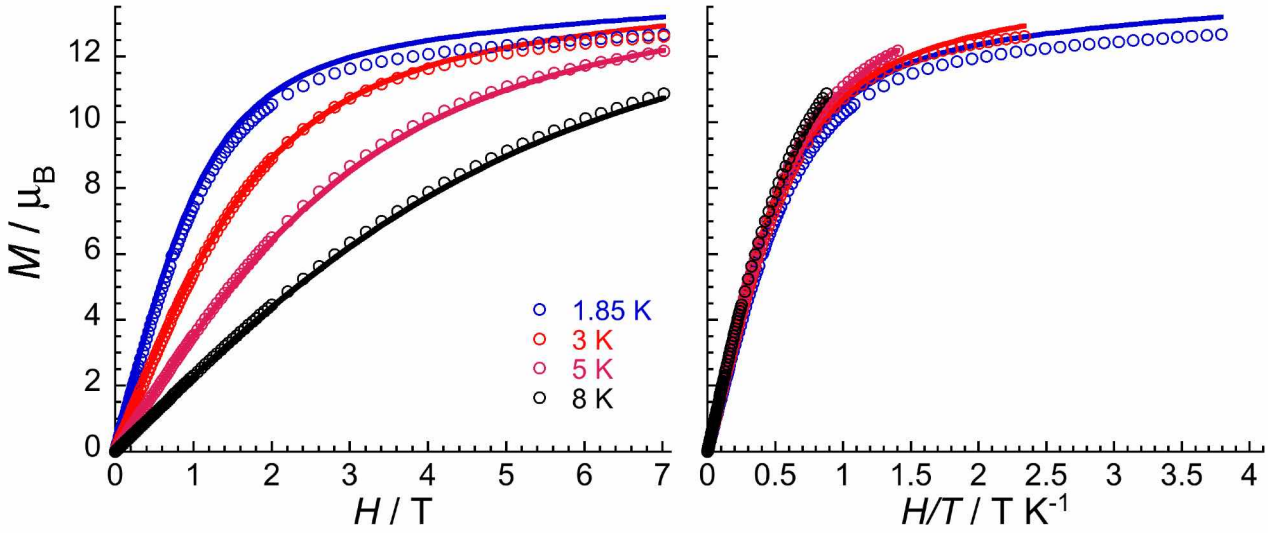

Figure S14. Field dependence of the magnetization, *M*, for **1** below 8 K (scanning at 10 – 40 mT.min^{-1} for $H < 1$ T and 50 – 250 mT.min^{-1} for $H > 1$ T) plotted as (left) *M* vs *H* and (right) *M* vs *H*/*T* plots. The solid lines are the best fit of the magnetization data to the model described in the main text.

AC Magnetic Data

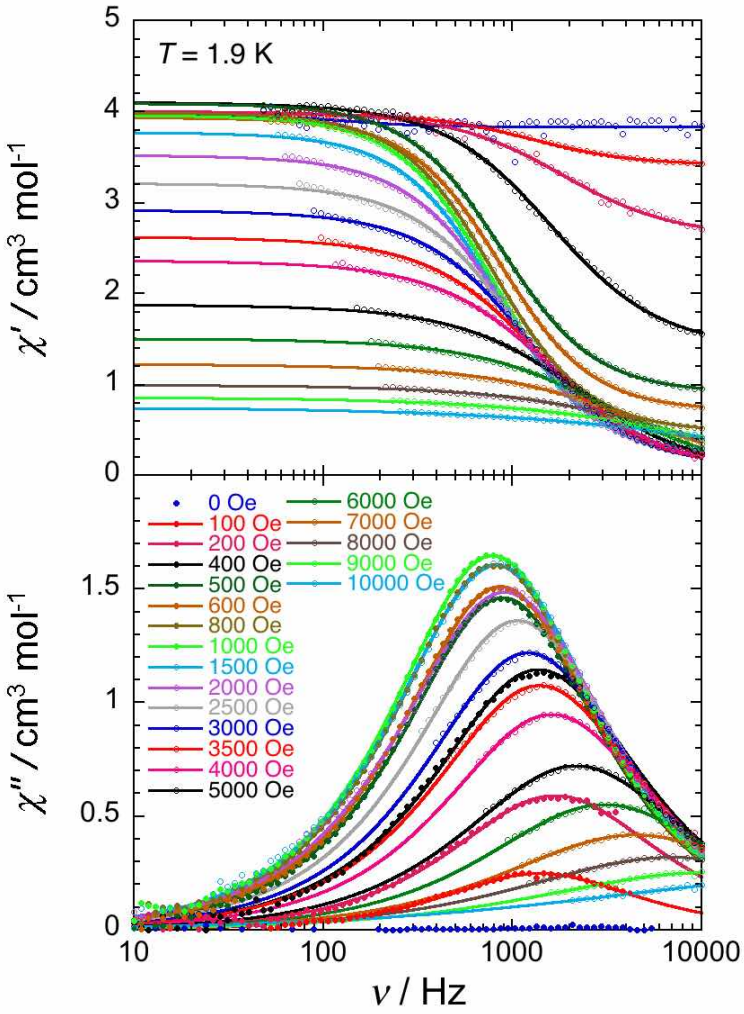

Figure S15. ac frequency dependence of the real (χ', top) and imaginary (χ'', bottom) parts of the ac susceptibility for **1**, at 1.9 K between 10 and 10000 Hz in dc-field between 0 and 10000 Oe. Solid lines are the generalised Debye fits[S10] of the ac data used to extract the field dependence of the relaxation time shown in Figure 4.

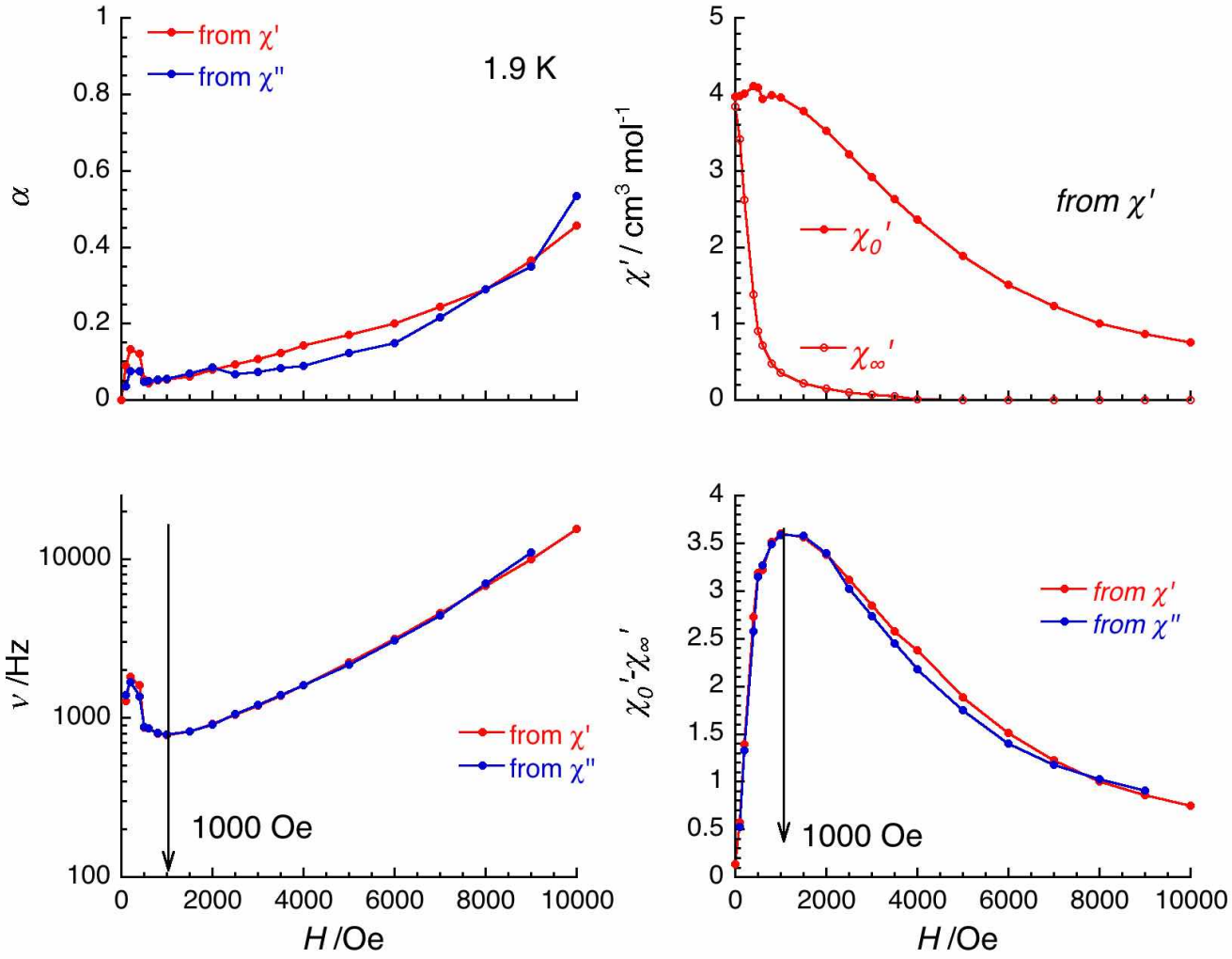

Figure S16. Field dependence of the parameters, α, ν, χ_0', χ_∞' and χ_0'-χ_∞', between 0 and 10000 Oe at 1.9 K deduced from the generalised Debye fit[S10] of the frequency dependence of the real (χ') and imaginary (χ'') components of the ac susceptibility shown in Figure S15, for **1**.

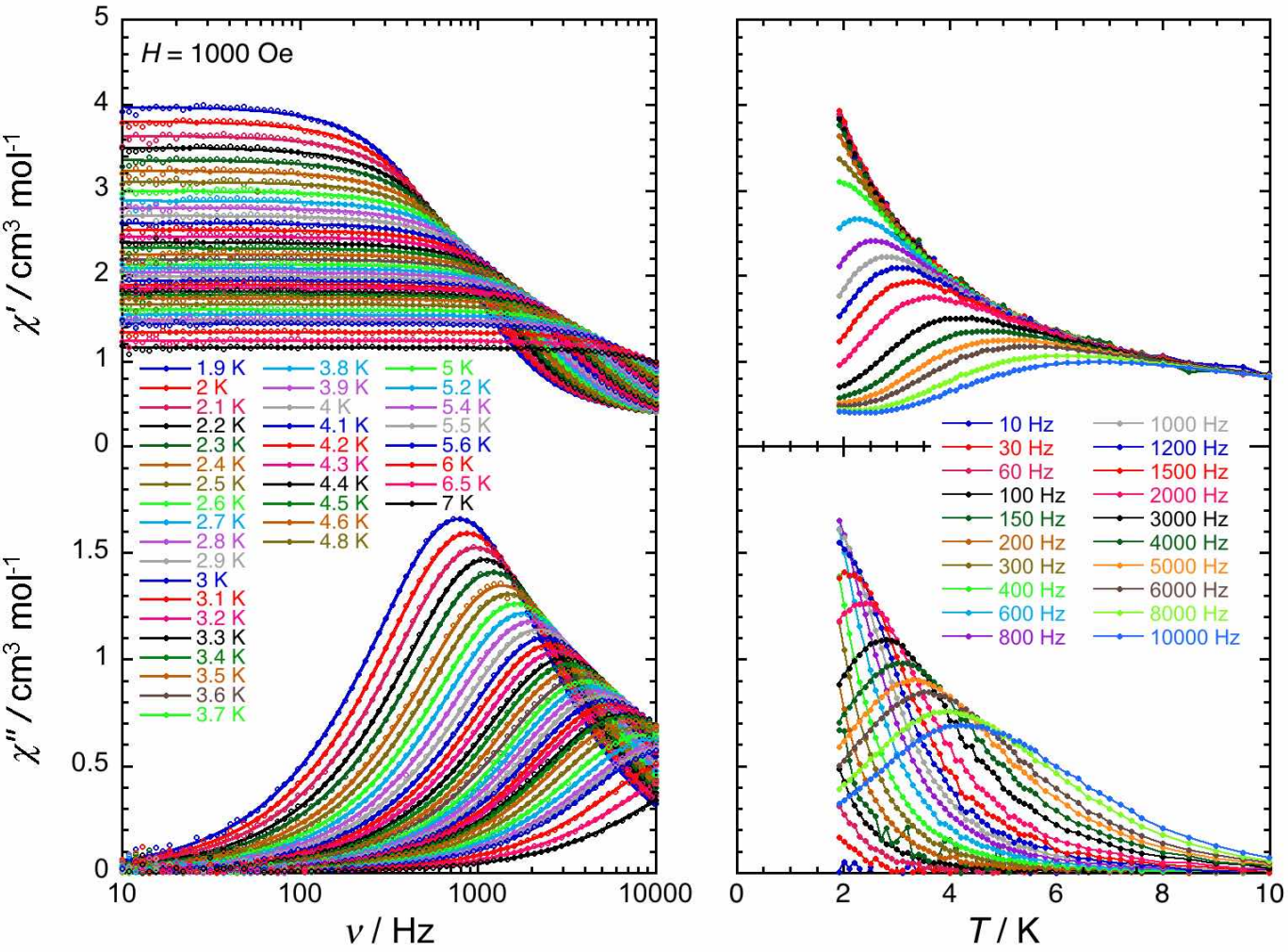

Figure S17. ac frequency (left) and temperature (right) dependences of the real (χ', top) and imaginary (χ'', bottom) parts of the ac susceptibility for **1** at 1000 Oe, for ac frequencies between 10 and 10000 Hz and between 1.9 and 10 K. Solid lines on the χ' vs. ν and χ'' vs. ν plots are the generalised Debye fits[S10] of the ac data used to extract the temperature dependence of the relaxation time (Figure 4) as well as α, ν, χ_0', χ_∞' and χ_0'-χ_∞' shown in Figure S18.

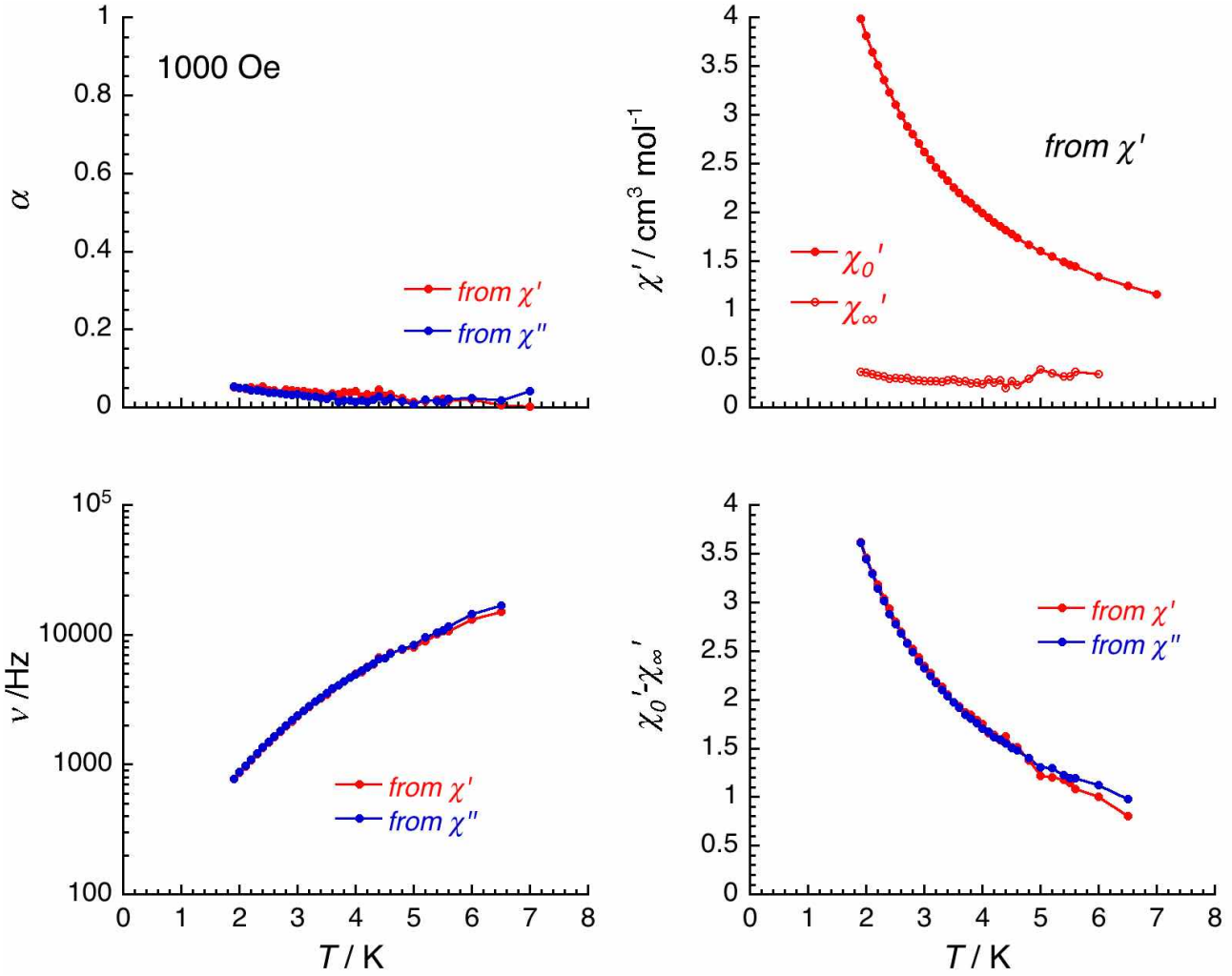

Figure S18. Temperature dependence of the parameters, α, ν, χ_0', χ_∞' and χ_0'-χ_∞', between 1.9 and 7 K at 1000 Oe deduced from the generalised Debye fits[S10] of the frequency dependence of the real (χ') and imaginary (χ'') components of the ac susceptibility shown in Figure S17, for **1**.

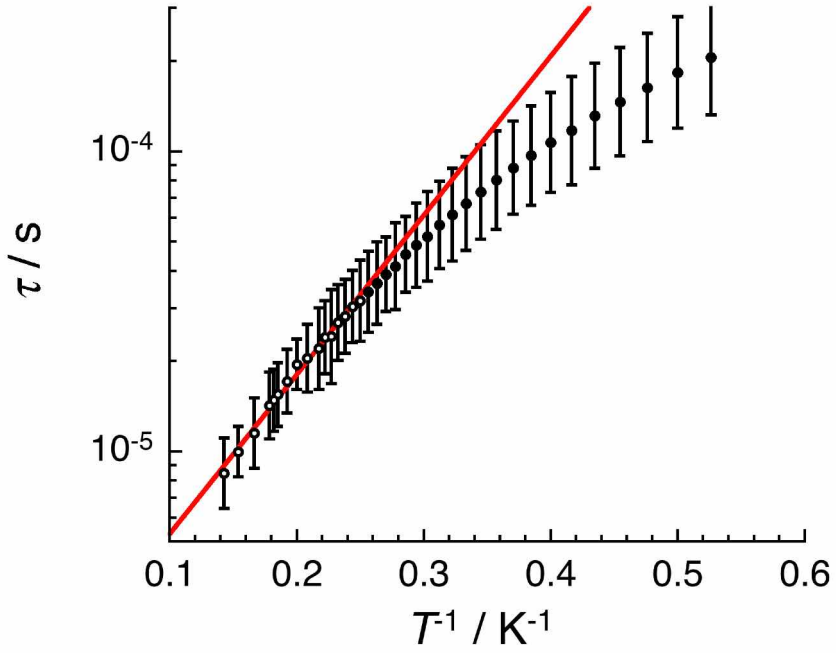

Figure S19. Plot of the average relaxation time (τ) vs. the inverse of the temperature (T^{-1}) between 1.9 and 7 K at 1000 Oe deduced from the generalised Debye fits[S10] of the frequency dependence of the real (χ') and imaginary (χ'') components of the ac susceptibility shown in Figure S17, for **1**. The estimated standard deviations of the relaxation time (vertical solid bars) have been calculated from the α parameters of the generalised Debye fit (Figures S17) and the log-normal distribution as described in reference S11. The solid red line is the best fit with an Arrhenius (thermally activated) law (with Δ/k_B = 12(2) K and τ_0 = 1.6(5) 10^{-6} s) considering the data above 4 K (open dots).

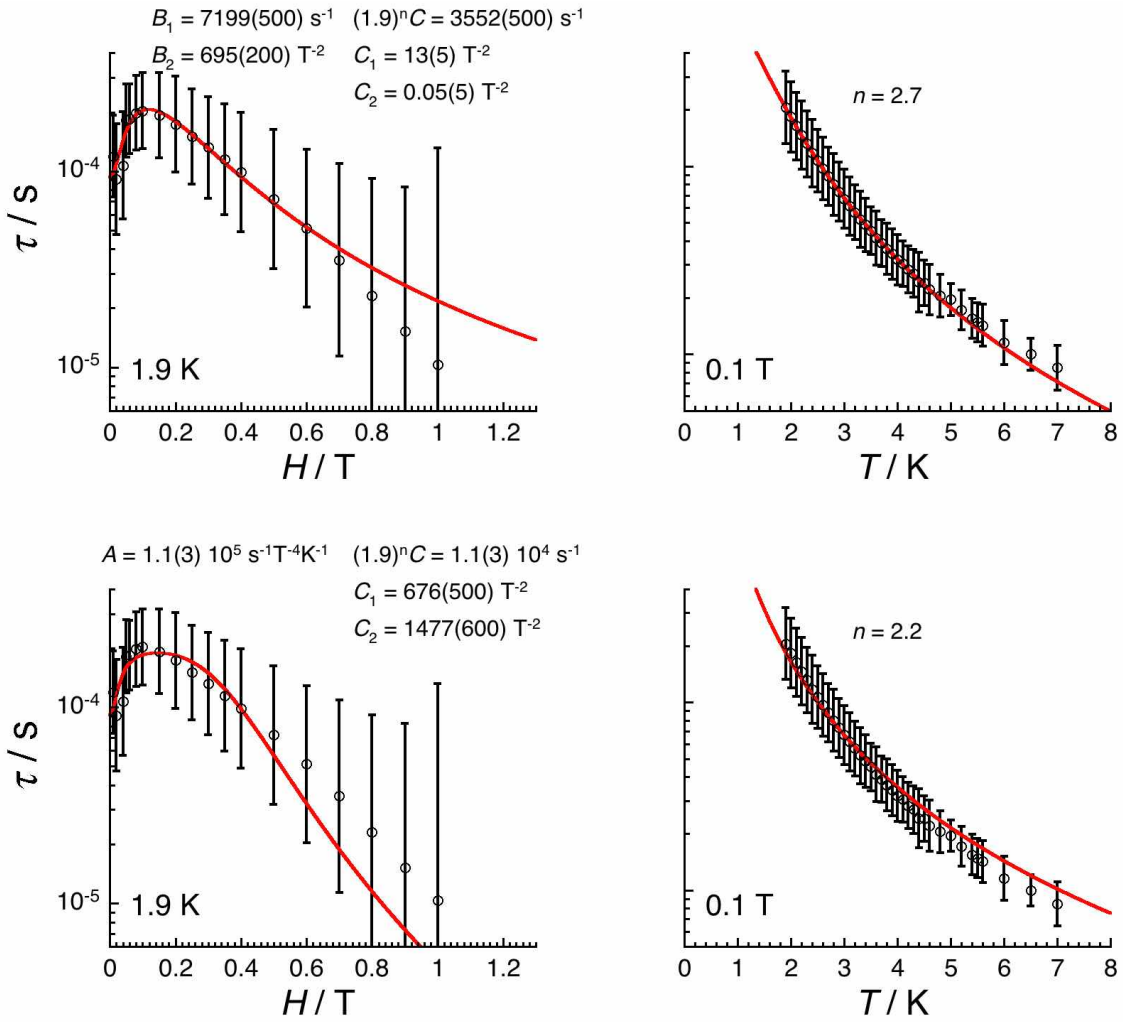

Figure S20. Field (left) and temperature (right) dependence of the relaxation time for **1** estimated from the generalised Debye fits[S10] of the ac susceptibility data shown in Figures S15 and S17. The estimated standard deviations of the relaxation time (vertical solid bars) have been calculated from the α parameters of the generalised Debye fits (Figures S15-S18) and the log-normal distribution as described in reference S11. The solid red lines are the best fit discussed in the text, including (top) quantum tunneling of the magnetization and Raman relaxation processes (Figure 4) and (bottom) Direct and Raman relaxation processes.

References

(S1) F. Weldon; L. Hammarström; E. Mukhtar; R. Hage; E. Gunneweg; J. G. Haasnoot; J. Reedijk; W. R. Browne; A. L. Guckian; J. G. Vos *Inorg. Chem.* **2004**, *43* (14), 4471.

(S2) CrysAlisPro, Agilent Technologies, Version 1.171.36.28

(S3) G. Sheldrick. *Acta Cryst. A.* **2015**, *71* (1), 3.

(S4) O. V. Dolomanov; L. J. Bourhis; R. J. Gildea; J. A. K. Howard; H. Puschmann, *J. Appl. Crystallogr.* **2009**, *42* (2), 339.

(S5) G. Sheldrick, *Acta Cryst. Sect. C* **2015,** *71* (1), 3-8.

(S6) CrysAlisPro, Agilent Technologies, Version 1.171.35.19; Empirical absorption correction using spherical harmonics, implemented in SCALE3 ABSPACK scaling algorithm.

(S7) P. van der Sluis; A. L. Spek *Acta Cryst. A* **1990**, *46*, 194

(S8) A. L. Spek, PLATON, A Multipurpose Crystallographic Tool, Utrecht University, Utrecht, The Netherlands, **2008**.

(S9) Marchivie, M.; Guionneau, P.; Létard, J.-F.; Chasseau, D. Towards direct correlations between spin-crossover and structural features in iron(II) complexes. *Acta Cryst. Sect. B* **2003**, *59*, 479-486.

(S10) K. S. Cole, R. H. Cole, *J. Chem. Phys* **1941,** *9* (4), 341.

(S11) D. Reta, N. F. Chilton, *Phys. Chem. Chem. Phys.* **2019**, *21*, 23567–23575.